

Berkeley
UNIVERSITY OF CALIFORNIA

Grenoble
phelma



UNIVERSITY OF CALIFORNIA, BERKELEY
MASTER'S THESIS

Design of a Molten Chloride Fast Spectrum Reactor

Author:
Louis GREGG

Supervisor:
Dr. Massimiliano
FRATONI

*A thesis submitted in fulfillment of the requirements
for the degree of Master of Science*

in the

**EMINE Program
Grenoble INP Phelma**

August 21, 2018

Acknowledgements

This project would not have been possible without the guidance and support of my supervisor, Professor Max Fratoni of the UC Berkeley Nuclear Engineering Department. In addition Ehud Greenspan's feedback on my preliminary simulation results was very helpful in informing my research questions and the methods undertaken to answer them. Michael Martin's patient and clear explanation of his work on the B&B mode of MSR's (which served as direct precursor and inspiration for this thesis) made replicating his results much easier. Discussions with Caroline Hughes, whose work also concerns B&B MCFR design, were very helpful throughout the study. Daniel Wooten provided invaluable tips and advice on various aspects of the project, from material damage to burnup definitions and MSR's in general. George Zhang enabled me to benchmark the DPA model in this project by kindly providing his FFTF and SFR flux data sets. He also provided clear guidance on how to build and use the DPA model. Tianliang Hu provided great insight into the cutting edge of MSR multi-physics modeling for transient scenarios and into MSR safety in general, which helped contextualize my efforts in the realm of neutronics. Jun Shi was very helpful in setting up my environment on the Savio computer cluster used in neutronics simulations in this work. Finally, I'd like to thank Chris Keckler, whose comprehensive knowledge of neutronics and astute engineering perspective improved all simulation experiments on which I sought his advice. Also he lent me a tent so I could go camping at Lake Tahoe.

I got to see a bear break into a Winnebago - it was awesome.

Contents

Acknowledgements	i
1 Socio-Economic Context	1
2 Introduction	8
2.1 Radiation Damage	8
2.2 Helium Production in Steel	10
2.3 Reactor Safety & the Temperature Reactivity Coefficient	11
3 Literature Review and Theoretical Background	13
3.1 UC Berkeley Burnup Studies	13
3.2 B&B MSR Studies Elsewhere	17
4 Experimental Method	19
4.1 Reactor Geometry	19
4.2 Radial Reflector Material	21
4.3 Radial Reflector Size Study	23
4.4 DPA Calculations	23
4.4.1 DPA Model Benchmark	24
4.5 Helium Production Calculation	27
4.6 Safety Calculations	27
4.6.1 The Combined Perturbation Method	29
4.6.2 The Separate Perturbation Method	29
4.7 Burnup Calculations	30
5 Results and Analysis	32
5.1 Radial Reflector Geometry	32
5.1.1 Radial Reflector Simulation Results	34
5.2 DPA Estimation / Component Lifetime Analysis	35
5.2.1 Reduced Plena Volume Simulations	38
5.3 Helium Production Results	39
5.3.1 Helium Build-Up Model Verification	39
5.3.2 HT9 Helium Production	42
5.4 Reactivity Coefficient Results	44
5.5 Discharge Burnup & Minimal Core Dimensions	46
5.6 Discharge Burnup and Reactor Safety	49
5.6.1 Lead-208 Safety Benefits	51
6 Discussion and Conclusions	53

Appendices	57
A Density Calculations	58
A.1 Lead Density Estimation	58
A.2 Chloride Salt Densities	58
A.3 HT9 Steel Density Estimation	58
B Core Volume & Power Calculations	60
Bibliography	62

List of Figures

1.1	CO ₂ emissions data for selected developed nations.	2
1.2	SWU per thermal energy output for the AP1000 and a B&BMSR, from [58].	6
3.1	k_{inf} and the neutron balance as a function of burnup in FIMA for the reference Sodium-cooled B&B core in [38].	13
3.2	A periodic table in which the elements are grouped according to the rate at which they were removed from the fuel material [1].	15
3.3	The k_{inf} for the equilibrium fuel composition for a range of feed/removal rates, from [58].	17
3.4	Core volumes necessary for criticality when using the equilibrium fuel composition [41].	17
4.1	Radial (left) and axial (right) cross sections of Reactor Geometry A, used as a benchmark in section 5.1 [58].	20
4.2	Radial (left) and axial (right) cross sections of Reactor Geometry B, conceived and simulated in this work.	20
4.3	Neutron energy spectra and histogram of damage-cross section data for HT9, produced using the SPECTER code documentation [35].	24
4.4	Neutron energy spectrum in the MCFR core. Histogram of damage-cross section data for HT9, produced using the SPECTER code documentation [35]. Seed-region SFR spectrum and SFR DPA cross section data provided by the authors of [84].	25
4.5	Neutron energy spectrum in the internal 5 cm of the MCFR reflector. Histogram of damage-cross section data for HT9, produced using the SPECTER code documentation [35]. reflector-region SFR spectrum and SFR DPA cross section data provided by the authors of [84].	26
5.1	Radial profile of Reactor Geometry B using 100 cm pure Lead (left) and steel-encased Lead (right) reflectors.	33
5.2	Criticality as a function of reflector thickness in geometry A.	33
5.3	Criticality as a function of reflector thickness in geometry B.	34
5.4	Radiation damage rate as a function of r and z position in the 20 cm 90% HT9/10% Salt reflector.	36
5.5	Macroscopic neutron cross-sections in a 90% HT9 / 10 % Fuel Salt reflector in Reactor Geometry B.	37

5.6	Radial cross sections of the power profile before and after the plena heights were reduced to 5 cm.	38
5.7	Neutron spectra in the 20-cm-thick 90% HT9 / 10 % Fuel Salt reflector in the MCFR and in the FFTF [84].	40
5.8	Average Helium build-up in the 90% HT9/10% Salt 20 cm reflector.	43
5.9	Helium concentration profile in the 90% HT9/10% Salt 20 cm reflector after 100 FPY.	44
5.10	The convergence to the equilibrium composition k_{eff} for various fuel-in-core residence times in the 230 cm radius core. . .	47
5.11	Equilibrium k_{eff} for Various Core Radii and Discharge Burnups. Criticality ($k_{eff} = 1$) indicated by the semi-transparent red plane.	48
5.12	The temperature reactivity coefficient for the equilibrium fuel compositions discussed in section 5.5.	50

List of Tables

4.1	Modifications made to Geometry B for each section in this thesis.	19
4.2	Chemical compositions and displacement energies for the steels used.	22
4.3	Various DPA-per-fast-fluence results for validation of the DPA calculation method.	25
4.4	Initial composition (by mass fraction) of the fuel used in burn-up simulations in sections 5.5 and 5.6.	31
5.1	Radial reflection saturation estimates for Reactor Geometries A and B.	35
5.2	Estimated component lifetimes, using a 208 DPA limit.	37
5.3	Component lifetimes with plena heights reduced to 5 cm, using a 208 DPA limit.	38
5.4	Maximum Helium concentrations after 100 full-power years (FPY).	43
5.5	Temperature-Reactivity coefficients obtained using the combined and separate perturbation methods in units of pcm K^{-1}	45
5.6	Extrema of the critical k_{eff} surface in figure 5.11 and the α_{temp} surface in figure 5.12.	49
B.1	Core volume and power information, with radii and volumes in m and m^3 , respectively.	61

List of Abbreviations

appm	atomic parts per million
ASME	American Society of Mechanical Engineers
at. %	atomic percentage
B&B	Breed and Burn
BBMSR / B&BMSR	Breed and Burn Molten Salt Reactor
BOO	Build-Own-Operate
BPVC	Boiler Pressure Vessel Code
BR	Breeding Ratio
CANDU	Canada Deuterium Uranium
CFD	Computational Fluid Dynamics
CIRUS	Canada India Reactor Utility Services
DC	Downcomer
DEMO	DEMONstration Power Station
DFT	density-functional-theory
DNS	Direct Numerical Simulation
DPA	Displacements Per Atom
FEM	Finite Element Methods
FFFER	Forced Fluoride Flow for Experimental Research
FFTF	Fast Flux Test Facility
FIMA	Fissions Per Initial Heavy Metal Atom
FPY	full-power years
GHGs	Greenhouse Gases
INDC	Intended Nationally Determined Contributions
IPCC	Intergovernmental Panel on Climate Change
LOCA	loss-of-coolant-accident
LOHS	Loss-Of-Heat-Sink
LP	Lower Plenum
LSI	Lower Steel Internals
LWR	Light Water Reactor
MCFR	Molten Chloride Fast Reactor
MCNP	Monte Carlo N-Particle Transport Code
MSFR	Molten Salt Fast Reactor
MSR	Molten Salt Reactor
NRC	Nuclear Regulatory Commission
NRT	Norgett, Torrens and Robinson
ODS	Oxide Dispersion Strengthened Steel
PCA	Prime Candidate Alloy
PIV	Particle Image Visualization

R&D	Research and Development
RANS	Reynolds-Averaged Navier Stokes
S&B	Seed and Blanket
SNF	Spent Nuclear Fuel
SRIM	Stopping and Range of Ions in Matter
SSR	Stable Salt Reactor
SWATH	Salt at Wall: Thermal Exchanges
SWUs	Separative Work Units
TWR	Traveling Wave Reactor
UP	Upper Plenum
USI	Upper Steel Internals
wt. %	weight or mass percentage

Dedicated to my Mother in the Old Country...

Chapter 1

Socio-Economic Context

The emission of greenhouse gases (GHGs), primarily CO₂ and methane, has produced a rise in global temperatures since the start of the industrial revolution. This anthropogenic global warming will have far-reaching impacts on the Earth's climate, the biosphere and on humanity. At the 2015 United Nations Climate Change / COP21 Conference in 2015, 195 countries committed to individual Intended Nationally Determined Contributions (INDCs) with the goal of limiting the increase in the global average temperature to 2°C above pre-industrial levels. Even in optimistic models which assume that developing nations radically limit their CO₂ emissions throughout periods of rapid economic growth, it's estimated that the United States must reduce its yearly GHG emissions by 80% of its 2000 levels by the year 2050 [55]. Similarly, the European Union (EU) has set a target of reducing carbon emissions to 80 to 95% below its 1990 levels by 2050 in its 2050 Low Carbon Roadmap [16]. However, even using optimistic assumptions on the future carbon emissions of developing economies, much doubt remains as to the efficacy of these carbon targets in limiting warming to 2°C. Indeed, the Intergovernmental Panel on Climate Change (IPCC) is currently working towards new INDCs with the goal of limiting warming to 1.5°C above pre-industrial levels [67] [17].

The scientific and governmental consensus is that the energy economies of developed nations must be rapidly decarbonized by phasing out existing fossil fuel plants, while simultaneously installing carbon-neutral energy capacity at unprecedented rates in both developed and developing economies. It is worth noting that the largest sustained national decarbonizations took place in Sweden and France in the 1970s and 1980s, almost entirely due to the ramp up of nuclear power. These efforts were driven by the political desire for increased energy security, partially in response to the 1973 Oil Crisis. It is worth noting that Denmark has produced similar reductions in CO₂ emissions through the rapid adoption of wind energy, by utilizing the high winds in the Baltic Sea region [67] [12].

These uniquely rapid rates of decarbonization are plotted in figure 1.1, with data obtained from the Carbon Dioxide Information Analysis Center [12], with Germany's CO₂ emissions data included for comparison.

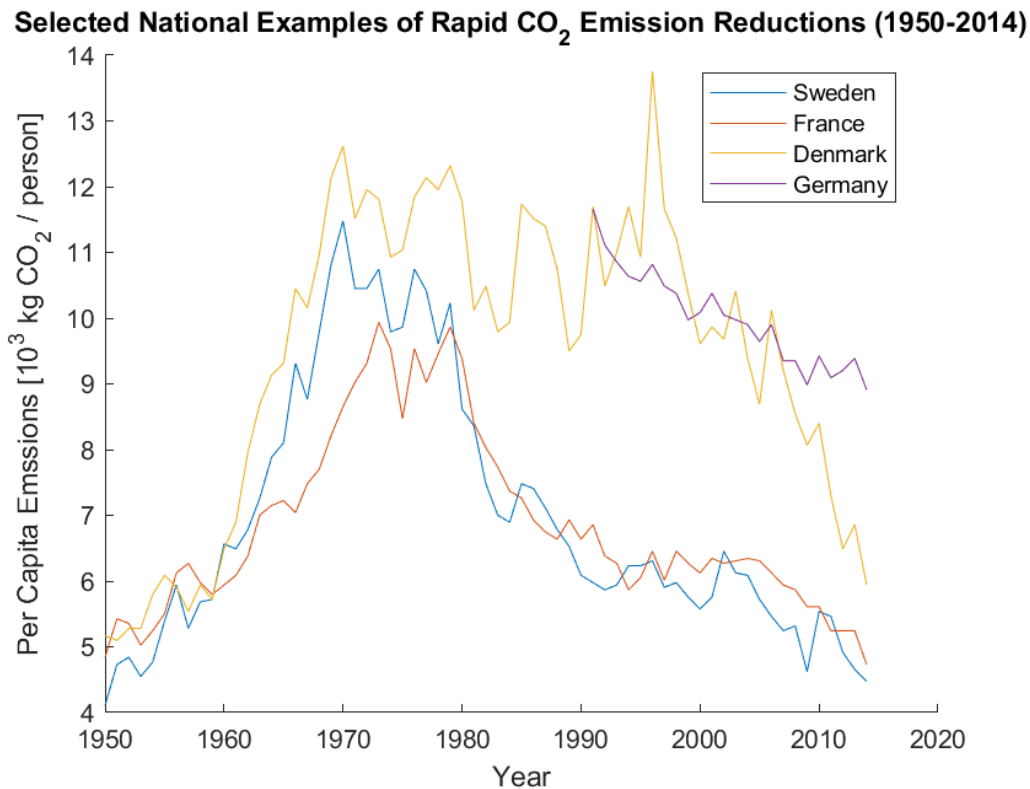


FIGURE 1.1: CO₂ emissions data for selected developed nations.

Despite substantial efforts under the *Energiewende* movement to subsidize renewable energy, German CO₂ emissions have been less drastically impacted than those of Denmark in a similar timeframe (see figure 1.1). The reduced efficacy of these efforts has numerous causes, including the low winds experienced in the south of the country and political opposition to nuclear power, particularly in response to the 2011 Fukushima Daiichi disaster. For example, electricity produced by nuclear power in Germany has fallen from 169.6 TWh in 2000 (representing 29.4% of all electricity consumed) to 97.1 TWh in 2014 (representing just 15.5% of all electricity consumed) [45]. This rapid nuclear phase-out has greatly hampered German efforts to reduce GHG emissions and will probably continue to do so in future, as the country currently plans to shut down all nuclear power plants by 2022 [26]. Considering the rapid decarbonization required to combat global warming and the limited success enjoyed by countries which reject nuclear power, it appears clear that the case studies of French and Swedish GHG reductions should not be ignored.

Given the rapid GHG emission reductions produced by France and Sweden in the 1970s and 1980s (see figure 1.1), many nations may wish to harness nuclear power, as part of a multifaceted effort to reduce carbon emissions which may also include Renewable Energy (RE), Carbon Capture and Storage (CCS), demand reduction and the electrification of transport. If nuclear

power is to be rapidly adopted as it was by some nations in the second half of the 20th century, then this increase in nuclear power production must be achieved in a safe, sustainable and economically-viable way.

While current reactor designs offer enhanced safety, with core melt frequencies (CMF) estimated to be $4.2 \times 10^{-7} \text{ year}^{-1}$ for the Westinghouse AP1000 and $6.6 \times 10^{-7} \text{ year}^{-1}$ for the European Pressurized Reactor (EPR) [72] [11], they achieve this with costly redundant-and-diversified active safety systems, passive safety systems and large containment buildings. In addition, Light Water Reactors (LWRs) have dual-purpose potential, in that they can be run on very short fuel cycles to produce Pu-239 in large amounts relative to other Plutonium isotopes, for use in nuclear weapons. These issues, among others, have led the members of the Gen-IV consortium to set the following goals for advanced reactor designs: sustainability, proliferation resistance, enhanced safety and economic feasibility [27]. In addition, they have identified 6 reactor designs as potential paths to achieving their ambitions. Perhaps the most technically ambitious of these designs, for which there is the least operational or experimental experience, is the Molten Salt Reactor (MSR).

Another important economic driver for nuclear R&D is enhanced fuel utilization, by means of closing the fuel cycle with breeder reactors and fuel reprocessing facilities. One study has estimated that Uranium reserves may run out by 2107 if current fuel consumption rates are maintained in an open fuel cycle or between 2059 and 2071 if the current increasing trends in consumption are linearly extrapolated [31]. However, to close the fuel cycle by means of reprocessing facilities is both costly and a proliferation risk using current technology. The sale of the Canada India Reactor Utility Services (CIRUS) and Canada Deuterium Uranium (CANDU) heavy-water-moderated reactors to India by Canada, ostensibly for peaceful purposes, allowed the Indian state to reprocess Plutonium from spent fuel to use in its first nuclear weapons test in 1974 [23] [20].

While this clandestine effort to produce weapons-grade material by a developing nation was made easier by the live-refueling feature of CANDU-type reactors, spent fuel from LWRs could also be used in this way, albeit at greater cost and less discreetly. Indeed, it is important to note that to reach high burnups using a fleet of solid-fuel reactors, reprocessing must be employed at some point in the fuel cycle to remove neutron poisons and address the effects of radiation creep, thermal creep and embrittlement in both the fuel pellets and cladding. Designs achieving higher burnups (typically of the order of 40% Fissions Per Initial Heavy Metal Atom or FIMA) have been proposed, by utilizing a breed-and-burn (B&B) fueling scheme, such as the CANDLE concept and Terrapower's Traveling Wave Reactor designs [73] [32].

However, these designs typically require cladding materials to withstand up to 500 Displacements Per Atom (DPA), whereas current steels have only

been validated up to 200 DPA [85] [32]. To achieve this high burnup goal and utilize depleted Uranium or Thorium as a feedstock while observing the radiation damage constraint of 200 DPA, seed-and-blanket (S&B) reactors have been proposed and studied [84]. Such designs offer a substantially reduced fuel cost per unit of electricity with almost 60% of the core power produced by the non-enriched natural Uranium or Thorium blankets in S&B designs. However they still represent a well-demonstrated proliferation vector, as Sodium-cooled fast reactors with breeding blankets have been used to produce weapons material in the past.

Although the source of French nuclear weapons material is secret, some suspect that Plutonium bred in the blankets of the Phenix and Superphenix reactors (rich in Pu-239) may have been reprocessed at the UP1 plant in Marcoule and used to modernize the French nuclear weapons stockpile [3] [71]. Whether or not this diversion of materials took place is less important than the fact that it would certainly have been technically feasible, given the reprocessing capabilities of the French state at the time. Superphenix could produce 330 kg of weapons-grade Plutonium per year in its blanket, or enough to produce roughly 60 tactical Nuclear warheads per year [14] [75]. Were the political climate to have changed drastically, the blanket material in the Phenix and Superphenix reactors could have been run on short burnup cycles to produce weapons materials very efficiently. Therefore we can conclude that a closed solid-fuel cycle utilizing breeding blankets and off-site fuel reprocessing represents an increased proliferation risk in comparison to conventional LWRs operated in an open fuel cycle.

Given the pressing need to expand nuclear power in both developing and developed nations to combat climate change and limit warming to 2°C or less by 2100, new nuclear technologies must be developed which are more economically competitive than current designs. To achieve the economic goals such designs must be inherently safe at lower cost, and they must make more efficient use of Uranium and Thorium resources. Finally, such designs must close the fuel cycle without increasing the proliferation risk when compared to current LWRs, which may preclude the use of breeding blankets to increase the overall conversion ratio (CR) of the reactor.

These goals are summarized quite succinctly in the goals of the Gen IV consortium [27] and MSR designs may represent the best way to meet all these goals at once. However, these reactors represent the most technically challenging of the Gen IV designs and the one for which there is the least construction, operations and decommissioning experience. In addition, many MSR designs, such as the MSFR, make use of a breeding blanket of salt which could present an enhanced proliferation risk for reasons discussed previously [56]. Therefore, some have begun to consider large-core, single-salt MSRs operated in a B&B mode, so called BBMSRs or B&BMSRs, as a potential pathway to achieving substantial savings in fuel enrichment costs, while simultaneously reducing the design's proliferation risk to the point that the reactor

could be exported to potential proliferators or nations in conflict-prone regions.

In a B&BMSR core, no separate breeding blanket is used which makes the design more proliferation-resistant than an MSR design with separate breeding / fuel loops. This is possible because a B&BMSR can achieve high breeding ratios (BRs) and burnups without reprocessing materials from the separate fertile-rich blanket. Reprocessing facilities represent a well-documented means of obtaining weapons-grade material, so to close the fuel cycle without one is very appealing from the perspective of the stated Gen-IV goals of enhanced proliferation resistance and sustainability (by reducing the amount of nuclear waste per unit energy) [27].

In a previous study conducted at UC Berkeley, the enrichment costs of the B&BMSR reactor were compared with those of the AP1000. The results are provided in figure 1.2, in Separative Work Units (SWU), as defined in equation 1.1. The SWUs associated with an enrichment process does not represent the energy consumed in enriching the material. Instead it represents the industrial effort associated with the enriching a load of material to a specified level. It is also directly proportional to the cost of the front end of a fuel cycle.

$$SWU = M_P V(x_P) + M_T V(x_T) - M_F V(x_F) \quad (1.1)$$

where

- M_F , M_P and M_T are the masses of the feed, product and tails Uranium streams.
- x_F , x_P and x_T are the concentrations of the feed, product and tails Uranium streams.

The $V(x)$ terms in the equation above represent the *value function* of the feed, product and waste streams, which is defined in equation 1.2.

$$V(x) = (1 - 2x) \ln \left(\frac{1 - x}{x} \right) \quad (1.2)$$

In producing figure 1.2, the authors simulated burnup calculations of a B&BMSR with 33% heavy metal content in the fuel and an initial Uranium enrichment of 11.2 wt. % for 2.08 years, the time required for reactivity to be recovered when the same reactor was fed with natural Uranium. SWU savings were observed after 5.91 years in comparison to the constant enrichment cost for operation of the AP1000. Eventually the B&BMSR would be fed with natural Uranium, when the fuel had reached the equilibrium composition. At this point fuel costs would become substantially less than those of conventional Light Water Reactors (LWRs). This fuel cycle would also reduce operational costs and the infrastructure required for smaller nations who wish to adopt nuclear energy.

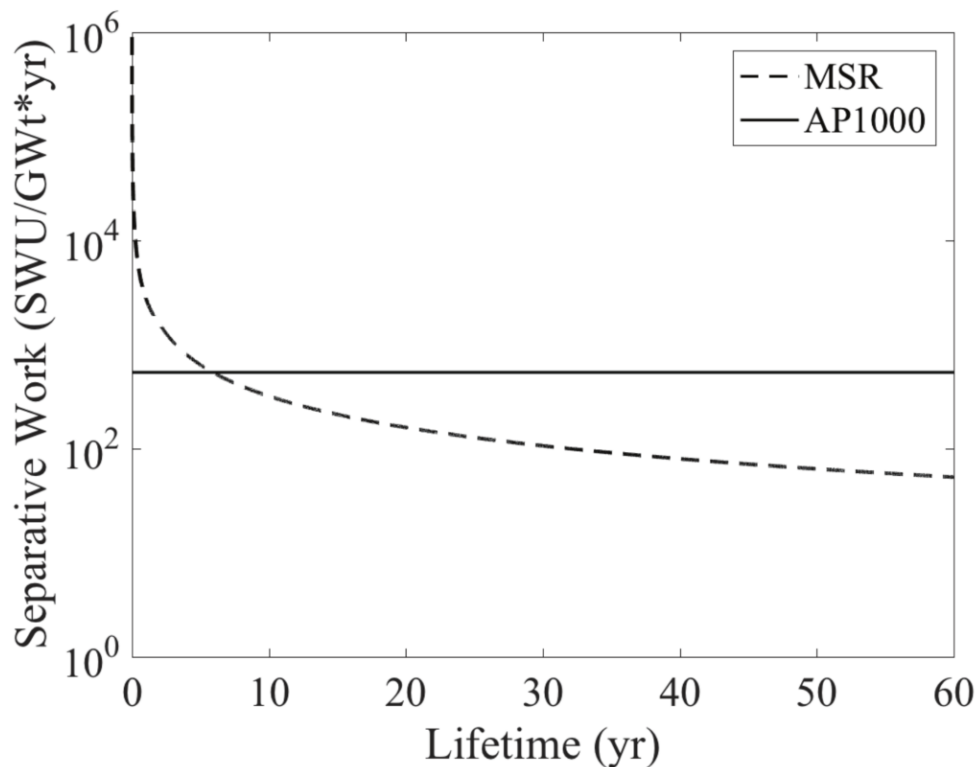


FIGURE 1.2: SWU per thermal energy output for the AP1000 and a B&BMSR, from [58].

It is important to note that the large core size required to achieve the B&B mode of operation adds substantially to construction costs and the overall capital costs of such a reactor. In the past, the high capital costs associated with nuclear construction projects has been problematic for nations and utilities wishing to obtain loans from risk-averse lenders. It is possible that the inherent safety of MSRs may negate this effect somewhat by reducing the need for active safety systems on-site, but this won't be clear unless one of these reactors is commercialized.

Although it appears that the proliferation risk is minimized by the B&BMSR concept, in that it achieves breeding and high burnups without reprocessing or blanket salts, this risk may be alternatively addressed by strictly controlling the management of enrichment and the reprocessing of Spent Nuclear Fuel (SNF). A subsidiary of Rosatom, the Russian state atomic energy corporation, has begun construction of a nuclear reactor in Akkuyu, Turkey using a strategy called Build-Own-Operate (BOO). In this approach, the plan will be financed, built, operated and decommissioned by Russia, under contracts which guarantee the sale of electricity to Turkish utilities at a fixed cost. The fuel will be supplied by Rosatom and eventually the SNF will be returned to Russia for reprocessing [2] [8]. This approach towards the fuel cycle represents a very low-cost strategy for developing nations wishing to utilize nuclear power while also minimizing the proliferation risk by centralizing enrichment and reprocessing capabilities to an established nuclear state. This

approach using proven technologies may prove more achievable in the short term, when the significant Research and Development (R&D) costs necessary to realize MSRs are taken into account.

While implementing a B&B fuel cycle in an MSR has much potential to meet the ambitious goals set out by the Gen IV consortium, much research must be done to determine whether these reactors are technically feasible. Motivated by the high-level policy and strategy goals outlined in this section, the goal of this study is to determine whether the B&B mode in a cylindrical MSR core remains practical when further detail is added to the geometry and other design constraints are taken into account. It is hoped that these results may elucidate the unique challenges and desirable attributes of the B&BMSR concept and guide further research in the development of safe, economical and sustainable nuclear power.

Chapter 2

Introduction

The primary research question addressed in this work is the following: If operating MSR in the B&B mode is theoretically possible, as implied in the literature [58] [47] [41], then is it practical to implement? This central question motivated the experiments and inquiries carried out in this study. In a cylindrical geometry with Lead reflector, the minimum core volume for B&B operation was found to be 30.87 m^3 , which corresponds to a thermal power of 9.26 GW, assuming a power density of 300 W cm^{-3} [58]. The largest existing LWRs are $\sim 1/3$ of this power rating. If we make the geometry more realistic than a simple cylinder, perhaps moving towards something similar to the working model of the MSFR [69], how will this affect the minimum core volume required to achieve B&B? In addition, how does radiation damage affect the lifetime of components if we impose the standard DPA constraints? How does the feed/removal rate of fuel salt from the core effect criticality, breeding ratio and overall feasibility? This investigation attempts to answer these questions using neutronics simulations in Serpent [54] in combination with modifications made to allow for a continuously changing fuel composition, as takes place in MSR [6].

2.1 Radiation Damage

The concept of Displacement-Per-Atom (DPA) is a widely-used standard for the quantification of molecular-level damage accrued in crystalline materials under irradiation by neutrons or other energetic charged particles. This quantity is defined as the ratio of the number of displaced atoms per volume as calculated by the NRT equation to the number of atoms in the same volume. The NRT model, so-called for its creators Norgett, Torrens and Robinson, is an evolution of the model suggested by Kinchin & Pease, which estimates the number of atoms displaced by an incident particle as a function of the energy of the incident particle and the displacement energy of the constituent atoms in the lattice. It is given in equation 2.1 as taken from [64]. The NRT model was proposed in [60] as an extension of the model for radiation damage proposed by Kinchin and Pease [48] [81].

$$N_d(T_d) = \begin{bmatrix} 0, & T_d < E_d \\ 1, & E_d < T_d < \frac{2E_d}{0.8} \\ \frac{0.8T_d}{2E_d}, & \frac{2E_d}{0.8} < T_d < E_c \\ \frac{E_c}{2E_d}, & E_c < T_d \end{bmatrix} \quad (2.1)$$

where:

- N_d is the number of displaced atoms produced by an incident neutron energy of T_d , in eV.
- E_d is the displacement energy of atoms in the lattice, usually taken to be 40 eV for Iron, Chromium and steels.
- E_c is the cut-off energy in eV, specific to the lattice. This is the incident neutron energy for which the number of displaced atoms saturate. For neutrons above this energy, neutron-electron interactions compete with neutron-nuclei interactions.

This equation uses a number of approximations, such as simplifying the recombination of defects or the saturation of defects in a particular region of the lattice. However it is widely used in nuclear engineering because, among other things, it can provide an order-of-magnitude estimate of material damage neutronic simulations. A method to compute the DPA in HT9 steel for a given neutron flux spectrum was used in this work to estimate the component lifetime of materials in the Molten Chloride Fast Reactor (MCFR), which is discussed in section 4.4. This was made possible by the readily-available DPA cross sections provided with the SPECTER code [35], developed by Argonne National Labs and adopted for DPA calculations in previous advanced reactor simulation studies [65]. While convenient to implement and well documented, these DPA cross sections were produced by computer codes developed in the 1980s, and are somewhat out-dated. For example the cross section data is for a limited set of elements, which conveniently include all of the principle nuclides of the HT9 steel used in this study. In addition the cross sections are discretized into only 100 energy groups. The substantial increase in scientific computing power that has been made since the 1980s could allow for higher fidelity damage energy cross sections to be developed for a larger set of elements. Perhaps in future works, more mature and actively maintained radiation damage tools such as the Stopping and Range of Ions in Matter (SRIM) [86] could be integrated with neutronics codes to more accurately gauge the effect of radiation damage on material properties. Indeed the NJOY Nuclear Data Processing System may be combined with neutronics codes to calculate damage in units of DPA [66] and the Monte Carlo N-Particle Transport Code (MCNP) has support for limited DPA estimation natively [82].

Samples of HT9 steel and other materials were subjected to a maximum radiation damage approximately of 208 DPA in the Fast Flux Test Facility (FFTF) experiments [80]. The material characteristics of ferritic-martensitic

steels are relatively favorable, demonstrating a swelling rate of $\sim 0.2\%/dpa$ in the 100 to 200 dpa range [24][28]. In contrast, austenitic stainless steels experience void-induced embrittlement at $\sim 10\%$ swelling, which severely limits their usage in high-radiation environments [28][63][4].

In any case, the FFTF-derived data represents the only material performance evaluation of steels subjected to fast-spectrum neutron-irradiation. Therefore this is the limit to which the swelling and embrittlement characteristics of HT9 steel in response to neutron irradiation can be reliably predicted. For this reason it has been used as a radiation damage limit in the design of fast reactors and it was used as such in this work [84].

2.2 Helium Production in Steel

The formation of Helium bubbles due to neutron irradiation embrittles steel by increasing the stresses along grain boundaries and increasing the tendency to inter-granular failure [22]. Helium bubbles are formed primarily due to neutron capture in ^{58}Ni , which has a natural abundance of 68.077 atomic percentage (at. %). A simplified version of this process is shown in equation 2.2 [9].



If we consider only neutron capture in Nickel as a source of Helium, then the rate of Helium production can be easily modeled for the steels used in our neutronic simulations. The capture and alpha-production cross sections of Nickel isotopes are highest in the thermal neutron region, so it was uncertain how pronounced the Helium-production effect would be in the fast spectrum of the MCFR.

The Helium production rate in ^{58}Ni in steel structural materials was estimated in this study using the following equation, originally developed by Argonne National Laboratory [34].

$$\frac{N(\text{He})}{N_0(^{58}\text{Ni})} = \frac{\sigma_\alpha}{\sigma_T} + \frac{\sigma_\alpha e^{-\sigma_\gamma \phi t}}{\sigma_\gamma - \sigma_T} - \frac{\sigma_\alpha \sigma_\gamma e^{-\sigma_T \phi t}}{(\sigma_\gamma - \sigma_T) \sigma_T} \quad (2.3)$$

where:

- $N(\text{He})$ is the number of Helium atoms produced.
- $N_0(^{58}\text{Ni})$ is the initial number of ^{58}Ni atoms.
- σ_α is the spectral-averaged microscopic cross section for the (n,α) reaction in ^{59}Ni .
- σ_T is the spectral-averaged microscopic total absorption cross section of ^{59}Ni .
- σ_γ is the spectral-averaged microscopic cross section for the (n,γ) reaction in ^{58}Ni .

- ϕt is the fluence experienced in time t .

2.3 Reactor Safety & the Temperature Reactivity Coefficient

The temperature-reactivity coefficient is the primary neutronic criterion used in the assessment of reactor safety. It quantifies the amount of reactivity inserted or removed by a temperature increase of 1 Kelvin. It is held to be an important standard for any reactor design that its temperature reactivity coefficient be negative, so as to minimize the reactivity inserted in design basis accidents (DBAs) such as the Loss-Of-Coolant-Accident (LOCA). Although MSRs differ greatly for conventional reactors in their governing physics, the temperature-reactivity coefficient remains an important measure of reactor safety. Indeed the single fluid coolant / fuel design creates an even greater and more instantaneous coupling between temperature and reactivity than in solid-fuel designs. Therefore one of the goals of this project was to calculate the temperature-reactivity coefficient for the MCFR and to ensure that it was negative. The methods for evaluating this parameter are documented in section 4.6, including measurements of uncertainty.

It is worth noting that evaluating the performance of MSRs under transient conditions is the subject of ongoing study, with many open questions to address. The influence of the drift of Delayed Neutron Precursors (so-called DNP drift) and the thermal hydraulics of the fuel salt introduce significant complexity to the behavior of MSR transients. In order to accurately model MSR accidents, several multi-physics models are under development. In order to achieve the necessary accuracy these models typically use Monte Carlo methods to simulate neutron criticality cycles, and Finite Element Methods (FEM) to simulate the fluid flow of the carrier salt. Both these methods have a relatively high computational cost associated with them, so many model simplifications are under consideration, particularly in regards to the granularity of turbulence modeling in the salt. Some researchers have concluded the Reynolds-Averaged Navier Stokes (RANS) and Direct Numerical Simulation (DNS) approaches are unique in offering an acceptable trade-off between computation cost and accuracy in modeling turbulence in the salt flow [70].

Many of these studies have made use of the Samofar project's Molten Salt Fast Reactor (MSFR) design as a standard benchmark to compare codes [69]. In addition to a benchmark reactor, these computational efforts must be validated by experimental data. Several experimental setups have been built or have been proposed to evaluate the thermal hydraulic behavior of the candidate molten salts. LiF-NaF-KF has been studied in the Forced Fluoride Flow for Experimental Research (FFFER) experiment [13]. The Salt at WALL: Thermal ExcHanges (SWATH) facility will consist of two experimental setups [70] and is designed specifically to develop the MSFR. SWATH-W, the first experimental setup, will verify the accuracy of Computational Fluid

Dynamics (CFD) models under development by performing Particle Image Visualization (PIV) to measure flow conditions in water. SWATH-S, the second experimental setup, will consist of a loop of LiF-NaF-KF salt, chosen for its similarity to the MSFR reference salt, LiF-Th₄. The Reynolds, Prandtl and Grashof numbers will be kept similar to those for LiF-Th₄ to allow for the study of the heat transfer and phase change properties in the MSFR.

MSRs undergo many unique physical processes in extreme and accidental conditions that must be understood to evaluate the safety of these designs. In an overcooling scenario, the fuel salt may solidify inside part or all of the heat exchangers, blocking the flow and potentially exacerbating the severity of the accident. The SWATH-S experiments may shed light on these processes. In addition, at very high temperatures such as in a Loss-Of-Heat-Sink (LOHS) scenario, the radiative term in the heat transfer equation for the salt becomes non-negligible. How this might effect an accident progression is currently unknown, as are the optical properties of the salt. The SWATH-S experiment may also provide valuable data on these topics.

Although the experiments outlined above will be very helpful in validating computational MSR models, many of the open questions highlighted are material-specific. Hence the usefulness of these results in determining the behavior of Chloride salts will be more limited, particularly in regards to accident scenarios. Indeed, Chloride salt experiments, equivalent to those designed to test the physics and chemistry of the MSFR, will eventually be necessary to make meaningful progress on the MCFR design.

Chapter 3

Literature Review and Theoretical Background

3.1 UC Berkeley Burnup Studies

The B&B fuel management concept is typically envisaged for large-core Sodium-cooled solid-fuel fast reactors. In the B&B mode, with the exception of the initial loading of enriched fuel to achieve criticality, the reactor is fueled exclusively with fertile material. In a B&B SFR design studied at UC Berkeley, this fertile fuel is placed in several radial blankets around a region of enriched fuel at the center of the core [84]. As the core runs to high burnups, each radial breeding blanket is shuffled inwards during refuelling as the concentration of Pu-239 and other fissile nuclides builds up in each radial layer. By combining this shuffling scheme with a melt-refining process applied to spent fuel ejected from the center of the core, the fuel can be used to high burnups, i.e. between 19.4% and 55% FIMA [40] [38].

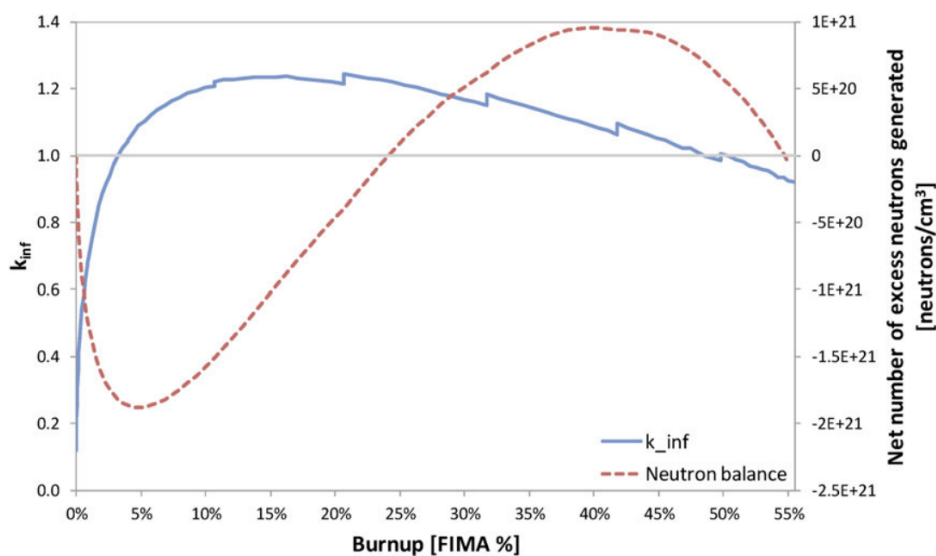


FIGURE 3.1: k_{inf} and the neutron balance as a function of burnup in FIMA for the reference Sodium-cooled B&B core in [38].

Figure 3.1 shows the evolution of criticality produced by a 0-D model of a breeding blanket zone in a B&B core. When the neutron balance is negative,

the region may be seen as a net *consumer* of neutrons. Therefore, this trend suggests that fissions in the blanket region must be driven by an external source up to FIMA values of $\sim 5\%$, at which point the blanket region may sustain criticality independently until it has compensated for the neutrons it had previously consumed, which occurs at $\sim 24\%$ FIMA. In the case of an actual B&B the 'external driver' up to FIMA=5% is fissile region at the center of the core. As fissile material is bred in the external blankets it is incrementally shuffled inwards where it may drive breeding in fresh fertile material in the new blankets - hence the name 'breed-and-burn'. This technique allows criticality to be sustained without using large volumes of enriched material as fuel, keeping fuel costs low.

The possibility of operating an MSR in the B&B mode has been a subject of study by several groups in recent years. In essence, rather than shuffling radially concentric breeding blankets inward as their fissile content increases, the core consists of a large volume of homogeneous salt, without a separate breeding blanket. The fuel salt is initially enriched to a moderate degree, e.g. to 11.2 at. % Pu-239 as used in this study. The core is then fed with enriched material (possibly of gradually decreasing enrichment) until the core may sustain criticality using the fissile materials which had been bred in-core. At this point the core may be fed with depleted or natural Uranium and no further enrichment or reprocessing is necessary to achieve high burnups, potentially in the range of 46 % FIMA for a total salt volume of 65 m³ using a steel reflector (see table 5.6 for details). Much work has been done to determine the technical feasibility of BBMSR designs and analyze their associated fuel cycles. Some previous studies which informed this work are summarized below.

A feasibility study of operating a Molten Chloride Fast Reactor (MCFR) in the B&B mode conducted at UC Berkeley was the main precursor to this masters thesis [58]. This study documented neutronics simulations conducted in the Monte Carlo code Serpent [54] with modifications to allow for the fuel composition to be gradually modified with time [6], for salt in an 'infinite' geometry, composed of a 1 cm⁻³ cube with reflective boundary conditions, and a cylindrical reactor geometry. In the infinite geometry simulations, the combination of Chloride salts utilizing a Uranium-Plutonium cycle was identified as permitting sufficiently high breeding ratios for the B&B mode to be achievable.

In the modified Serpent code the elements in the fuel were divided into three groups. A periodic table of elements with these groups highlighted, kindly provided by Caroline Hughes, can be found in figure 3.2. Each group of elements was removed from the fuel with a specific time constant defined in the code [1] [6]. This grouping scheme was intended to roughly approximate the chemistry of each group in combination the extraction rate of the fuel. Gaseous elements and heavy metals (in yellow) were removed from the core with a fixed in-core half-life of 30 minutes. Light elements with atom

hydrogen 1 H 1.0079																	helium 2 He 4.0026																		
lithium 3 Li 6.941	beryllium 4 Be 9.0122											boron 5 B 10.811	carbon 6 C 12.011	nitrogen 7 N 14.007	oxygen 8 O 15.999	fluorine 9 F 18.998	neon 10 Ne 20.180																		
sodium 11 Na 22.990	magnesium 12 Mg 24.305											aluminum 13 Al 26.982	silicon 14 Si 28.086	phosphorus 15 P 30.974	sulfur 16 S 32.065	chlorine 17 Cl 35.453	argon 18 Ar 39.948																		
potassium 19 K 39.098	calcium 20 Ca 40.078	scandium 21 Sc 44.956	titanium 22 Ti 47.867	vanadium 23 V 50.942	chromium 24 Cr 51.996	manganese 25 Mn 54.938	iron 26 Fe 55.845	cobalt 27 Co 58.933	nickel 28 Ni 58.693	copper 29 Cu 63.546	zinc 30 Zn 65.38	gallium 31 Ga 69.723	germanium 32 Ge 72.64	arsenic 33 As 74.922	seelenium 34 Se 78.96	bromine 35 Br 79.904	krypton 36 Kr 83.798																		
rubidium 37 Rb 85.468	strontium 38 Sr 87.62	yttrium 39 Y 88.906	zirconium 40 Zr 91.224	niobium 41 Nb 92.906	molybdenum 42 Mo 95.96	technetium 43 Tc [98]	ruthenium 44 Ru 101.07	rhodium 45 Rh 102.91	palladium 46 Pd 106.42	silver 47 Ag 107.87	cadmium 48 Cd 112.41	indium 49 In 114.82	tin 50 Sn 118.71	antimony 51 Sb 121.76	tellurium 52 Te 127.60	iodine 53 I 126.90	xenon 54 Xe 131.29																		
caesium 55 Cs 132.91	barium 56 Ba 137.33											hafnium 72 Hf 178.49	tantalum 73 Ta 180.95	tungsten 74 W 183.84	rhenium 75 Re 186.21	osmium 76 Os 190.23	iridium 77 Ir 192.22	platinum 78 Pt 195.08	gold 79 Au 196.97	mercury 80 Hg 200.59	thallium 81 Tl 204.38	lead 82 Pb 207.2	bismuth 83 Bi 208.98	polonium 84 Po [209]	astatine 85 At [210]	radon 86 Rn [222]									
francium 87 Fr [223]	radium 88 Ra [226]											rutherfordium 104 Rf [261]	dubnium 105 Db [262]	seaborgium 106 Sg [266]	bohrium 107 Bh [264]	hassium 108 Hs [268]	meitnerium 109 Mt [268]	darmstadtium 110 Ds [271]	roentgenium 111 Rg [272]																
																		lanthanum 57 La 138.91	cerium 58 Ce 140.12	praseodymium 59 Pr 140.91	neodymium 60 Nd 144.24	promethium 61 Pm [145]	samarium 62 Sm 150.36	europium 63 Eu 151.96	gadolinium 64 Gd 157.25	terbium 65 Tb 158.93	dysprosium 66 Dy 162.50	holmium 67 Ho 164.93	erbium 68 Er 167.26	thulium 69 Tm 168.93	ytterbium 70 Yb 173.05	lutetium 71 Lu 174.97			
																		actinium 89 Ac [227]	thorium 90 Th 232.04	protactinium 91 Pa 231.04	uranium 92 U 238.03	neptunium 93 Np [237]	plutonium 94 Pu [244]	americium 95 Am [243]	curium 96 Cm [247]	berkelium 97 Bk [247]	californium 98 Cf [251]	einsteinium 99 Es [252]	fermium 100 Fm [257]	mendelevium 101 Md [258]	nobelium 102 No [259]	lawrencium 103 Lr [262]			

FIGURE 3.2: A periodic table in which the elements are grouped according to the rate at which they were removed from the fuel material [1].

with atomic number up to 20 (in white), included the carrier salt components of Sodium and Chlorine, were held roughly constant over the course of the simulation. This ensured that the molar fraction of the carrier salt elements were held constant as the rest of the fuel composition evolved. Heavy metals and fission products (in green) were removed continuously from the fuel salt and replaced with natural Uranium, as defined by the LAMf2 variable and discussed below. The atomic density of actinides was held constant over the course of each burnup run. However, as the burnup simulation progressed the total atomic density of the fuel would increase with the build-up of soluble fission products until converging to the equilibrium composition. Hence the atomic *fraction* of actinides would also decrease and converge. In a sense, the equilibrium composition represented the state in which the rate of production of fission products was in balance with their removal from the fuel. This equilibrium fuel composition was primarily determined by the feed/removal rate.

Twenty cases representing twenty different fuel removal rates as defined as the variable LAMf2 in the eqlmc.h header file were simulated. The 20 cases were run to large burnups, usually 92,501 days or 15,346.8 MWd/kgU, to ensure that the fuel composition and k_{eff} had converged to some reasonably constant value. The only criteria for convergence in this case, was that k_{eff} no longer changed significantly with increasing burnup-days. At this point the fuel composition was considered to be at the equilibrium composition for the feed/removal rate specified.

Although each case was run to the same Serpent burnup in burnup-days, the discharge burnup (in FIMA) was different for each of the 20 cases, due to the different feed/removal rates. This LAMf2 variable was used to define the removal time constant for the salt in units of s^{-1} . It is defined analogously to the decay constant in radioactive decay, as shown in equations 3.1 and 3.2.

$$\frac{dN}{dt} = -\lambda_{removal} \times N \quad (3.1)$$

and

$$\lambda_{removal} = \frac{\ln(2)}{T_{1/2}} = \frac{1}{\tau} \quad (3.2)$$

where

- N is the number of fuel atoms.
- t is the time in seconds.
- $\lambda_{removal}$ is the removal time constant.
- $T_{1/2}$ is the in-reactor half life of fuel atoms.
- τ is the mean in-reactor lifetime for fuel atoms.

The discharge burnup is directly proportional to the residence time of the salt and can be determined in FIMA, according to equation 3.3.

$$FIMA = \frac{F\tau}{F\tau + N_{act}} \quad (3.3)$$

where

- F is the fission rate density of the equilibrium fuel composition in $cm^{-3}s^{-1}$.
- τ is the average residence time of fuel in the reactor in seconds. This can also be interpreted as the time required to completely re-fill the reactor with feed material.
- N_{act} is the number density of actinides in the equilibrium fuel composition.

Once each of the 20 removal time constant simulations had converged to a constant k_{inf} this converged, equilibrium-fuel-salt k_{inf} value was plotted as a function of FIMA, as shown in figure 3.3. This process was completed for three values of atomic fraction of heavy metals in the salt: 33%, 40% and 50%. The converged equilibrium fuel composition corresponding to the highest k_{eff} value in the 50% heavy metal line in figure 3.3 was used in this study to study the neutronic behavior of the optimum equilibrium fuel salt in various reactor geometries.

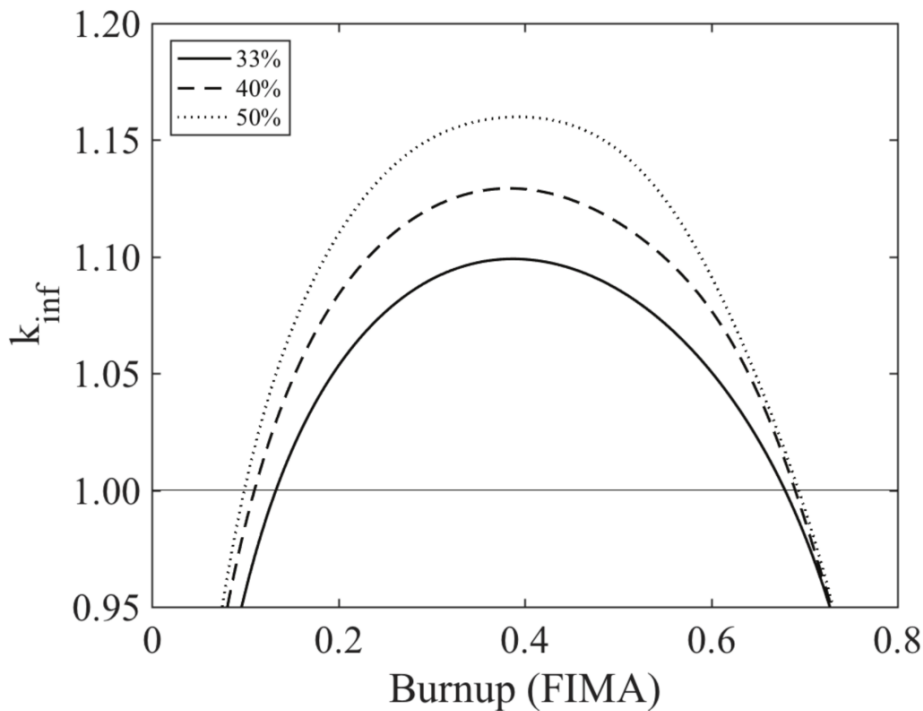


FIGURE 3.3: The k_{inf} for the equilibrium fuel composition for a range of feed/removal rates, from [58].

3.2 B&B MSR Studies Elsewhere

Another study approached the design with a goal of determining the burnups achievable, in units of FIMA, for a variety of carrier salts, fuels and reflector materials [41]. This work also quantified the minimum core sizes necessary to achieve the B&B mode when using several molten salt and reflector materials, as shown in figure 3.4. The data presented was for a cylindrical reactor with a height-to-radius ratio of 1.84 and a 100 cm reflector extending in all directions.

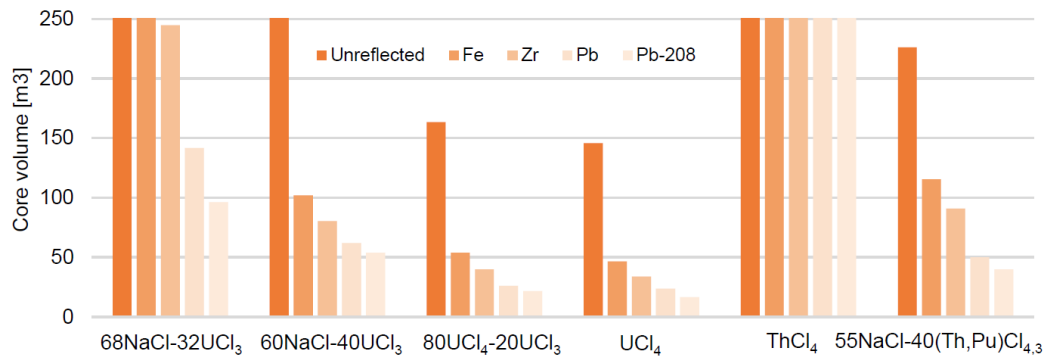


FIGURE 3.4: Core volumes necessary for criticality when using the equilibrium fuel composition [41].

From the results of this study, it can be seen that the core volume criteria was minimized when using Lead enriched to 100% Pb-208 as a reflector, with natural Lead offering the second-best performance. These results, in combination with the qualification of the performance of certain steels to high levels of irradiation influenced the decision to select Lead, HT9 steel and 316 steel for use as candidate reflector materials in this study.

Figure 3.4 also allows the comparison of several carrier salts, demonstrating that Chloride salt and Sodium-Chloride salts minimized the core volume parameter when reflector material was held constant. This result reinforced our decision to choose Chloride salts as the candidate carrier salt in exploring the practicality of the BBMSR reactor design.

Technical challenges in the operation and maintenance of MSR designs have led some to consider a design named the Stable Salt Reactor (SSR) in which molten salt is encased in cladding tubes, to further reduce the risk of radioactive contamination due to coolant leaks [62]. A feasibility study on implementing a B&B scheme in a reactor of the type under development by MOLTEX concluded that such a scheme may be best achieved by using a low-enriched Uranium equilibrium feedstock to insert reactivity and compensate for neutron losses in the coolant salt [47]. This would increase the fuel costs but may lead to significantly reduced capital costs by reducing the core size necessary to achieve B&B mode in an SSR-type reactor or in the homogeneous cylindrical core design studied here.

Chapter 4

Experimental Method

4.1 Reactor Geometry

In all simulations, the active core was treated as a cylinder of molten salt with a height-to-diameter ratio of 1. Core radii, reflector thicknesses and other details are summarized and sorted by study and section in table 4.1.

The fuel salt composition used in sections 5.1.1 to 5.4 was obtained via private communication from the authors of [58], and consisted of the equilibrium B&B fuel composition for a feedstock of $(\text{NaCl} + [\text{FP}]\text{Cl}_3) - [\text{Actinides}]\text{Cl}_3$ of molar proportions 50%-50% for which k_{eff} was highest. The equilibrium fuel composition was produced by running long burnup simulations in a version of Serpent specifically modified for modeling the evolution of fuel compositions in MSR [6]. This combination of this equilibrium fuel composition and reactor geometry produced the minimum core volume necessary to achieve criticality when using a 316 steel reflector of thickness 100 cm, which was present in both the axial and radial directions [58]. An example of this geometry, with the reflector in blue and fuel-salt in green, can be seen in figure 4.1. This core, taken directly from [58] shall be referred to as **Reactor Geometry A**, for clarity.

One of the goals of this thesis was to iteratively develop a reactor geometry, in an effort to simulate a more realistic and practical design than the simple cylinder in Reactor Geometry A. An image of the reactor geometry developed over the course of this thesis can be seen in figure 4.2 and shall be called **Reactor Geometry B**.

Study	Section	r_{core} [cm]	V_{core} [m ³]	$d_{reflector}$ [cm]	Reflector Material	UP [cm]	LP [cm]
Reflector-Reactivity	5.1	225	71.57	0-200	HT9/316/Lead	50	20
DPA Lifetimes	5.2	170	30.87	20	HT9	50 / 5	20 / 5
He Embrittlement	5.3	170	30.87	20	HT9	50	20
Safety Coefficient	5.4	170	30.87	20	HT9	50	20
Burnup/Core Radius	5.5	150-300	see table B.1	20	HT9	5	5
Burnup/Safety	5.6	150-300	see table B.1	20	HT9	5	5

TABLE 4.1: Modifications made to Geometry B for each section in this thesis.

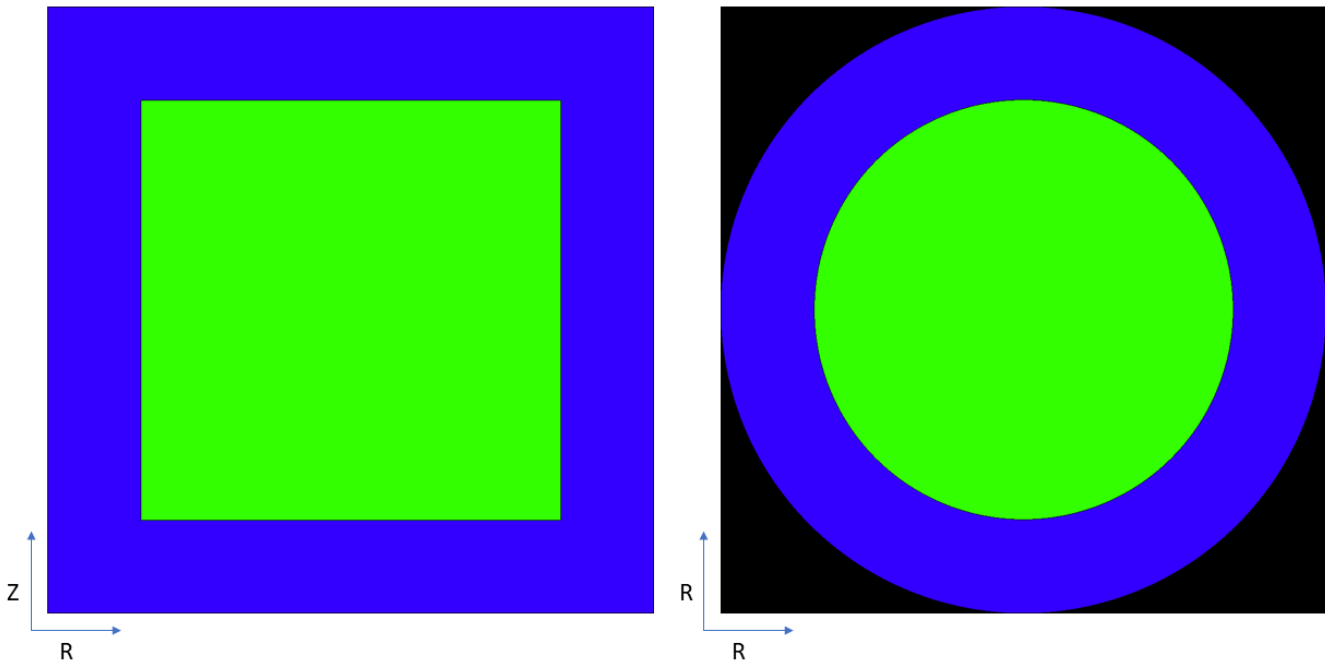


FIGURE 4.1: Radial (left) and axial (right) cross sections of Reactor Geometry A, used as a benchmark in section 5.1 [58].

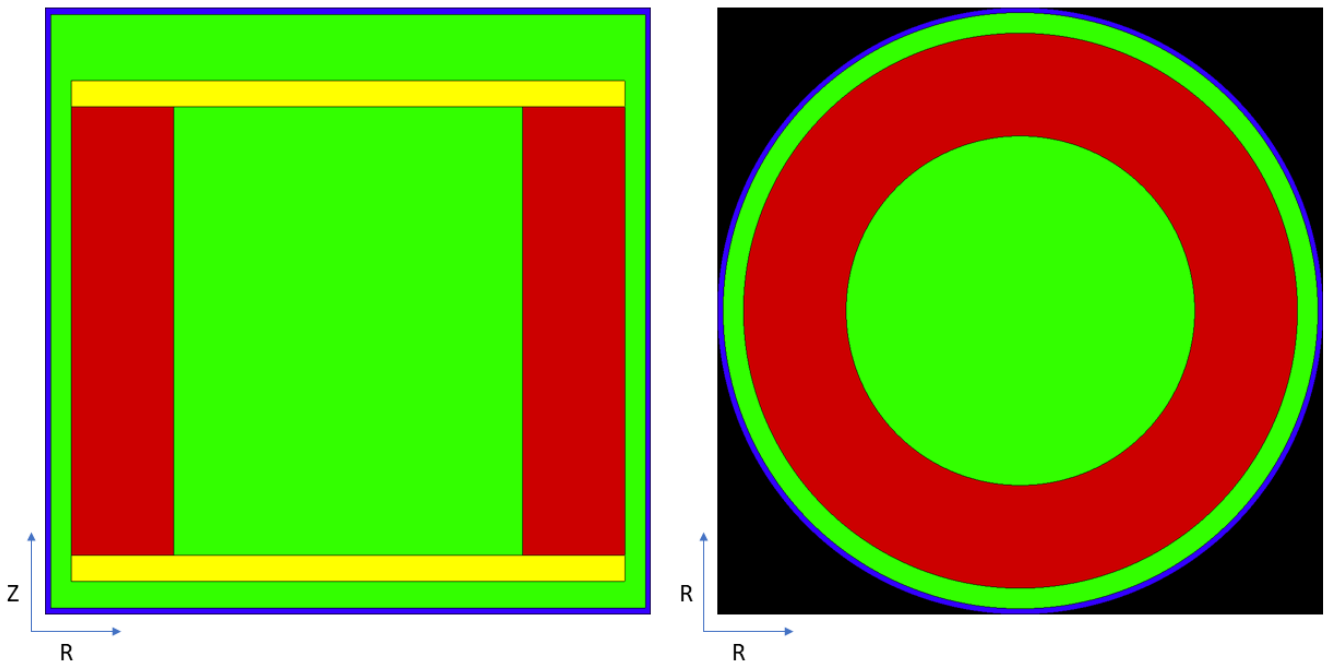


FIGURE 4.2: Radial (left) and axial (right) cross sections of Reactor Geometry B, conceived and simulated in this work.

The axial reflectors in Reactor Geometry A were replaced with a region of 50% steel / 50% fuel by volume, to represent internal steel components, such as flow channels, a core support structure and pumps. The height of these upper and lower steel component regions, shown in yellow in figure 4.2, were fixed at 20 cm above and below the core for all simulations. By replacing axial reflectors with a smaller region of mixed steel and salt, the axial reflection of neutrons was decreased. This meant that Reactor Geometry B core would be slightly less critical than Reactor Geometry A, in which the reflector completely encapsulated the core. Despite this, the core volume was held constant to isolate the influence of the radial reflector thickness on criticality from other variables.

The ex-core salt regions consisted of a 20 cm thick downcomer (DC), a 50 cm thick upper plenum (UP) and a 20 cm thick lower plenum (LP). For the DPA and burnup simulations detailed in sections 5.2.1, 5.5 and 5.6 both plena heights were reduced to 5 cm each in order to reduce the contribution of ex-core fissions to radiation damage in steel internals. This change can be seen in figure 5.6. The reactor vessel was a 5 cm of steel (in blue), which encased the downcomer and both plena. The material composition of the radial reflector region (in red) was varied, as discussed in the next section.

4.2 Radial Reflector Material

Important initial design decisions to be made include the choice of reflector size, shape and material. From a neutronics perspective it is desirable for the reflector to be made from a material with high atomic mass, high atomic density and low neutron capture cross-section. These qualities would ensure that the reflector softened the neutron energy spectrum as little as possible, reflected a high percentage of incident neutrons back towards the core while minimizing parasitic absorptions. Natural lead has many of these desirable properties and was chosen for a series of simulations as a result.

However, the high mass density of Lead would be a significant drawback during reflector maintenance and replacement. Moreover, given the low melting temperature of Lead at 600.6 K, requiring it to be encased in a corrosion-resistant steel casing in the core. This was modeled as a 5 cm layer of HT9 steel encasing the liquid Lead in the radial reflector. These materials issues, as well as the seismic risk associated with such a heavy reflector material, could render the Lead-reflector design to be impractical, despite its neutronic advantages.

Stainless steel reflectors would remain solid in the operating temperature range proposed for MCFRs and would be substantially less heavy. However being composed of lighter nuclides they would, in general, be more moderating as a reflector material than Lead. In addition, parasitic neutron absorptions by steels containing Molybdenum arise due to the high thermal capture cross-section of Molybdenum-95 (natural abundance = 15.87%, $\sigma_{\text{abs, thermal}} \approx 12.58$ barn) [42].

TABLE 4.2: Chemical compositions and displacement energies for the steels used.

Steel	HT9	316 (as in [58])	
ρ (g cm ⁻³)	7.67	8	
Element	Mass %		E_d [eV]
Cr	12	18	40
C	0.2	0.08	31
Mo	1	3	60
V	0.5	-	40
Mn	0.2	2	40
Si	0.25	1	25
Ni	0.5	13.845	40
P	-	0.045	-
S	-	0.03	-
W	0.5	-	90
Fe (Balance)	84.85	62	40

Two steels were chosen to compare the neutronic performance of steels with Lead: HT9 and the 316-type steel composition used in the study preceding this one, as a benchmark [58]. HT9 was chosen due to its qualification up to 200 DPA in the FFTF experiment and its comparability with molten salts [25]. In addition, the change of the mechanical properties of HT9 steel under irradiation has undergone the most testing and scrutiny of all candidate fast reactor materials [15]. The chemical composition of HT9 was obtained from the literature [53] and the density was calculated to be 7.67 g cm⁻³, using density equations obtained from [44] (see Appendix A.3 for details). The chemical compositions used in the Serpent simulations are tabulated in table 4.2.

Any steel present in the reactor would be subject to a substantial fast neutron flux which would heat the steel components due to the inelastic scattering of neutrons in the material. Therefore, one must consider the inclusion of cooling channels through the reflector, to allow heat removal by the molten salt fuel. To account for this, the annular reflector region around the active core in Reactor Geometry B was modeled as 90% steel/10% fuel-salt by volume, for all steel-reflected simulations.

For the use of a Lead reflector in Reactor Geometry B, two scenarios were simulated. To isolate the reflection effect of pure Lead, a reflector comprised of Lead, without casing was simulated. However to account for the fact that liquid Lead would need to be encased in a solid tank at the likely operating temperatures of the reactor, a second set of simulations were run in which the Lead reflector body was encased in 5 cm of HT9 steel. This represented a more realistic, albeit less neutronically favorable, scenario.

4.3 Radial Reflector Size Study

In order to determine the minimum thickness necessary to effectively reflect neutrons back to the active core, a series of Serpent simulations were carried out for various reflector thicknesses and materials. These simulations were conducted for both Reactor Geometry A and B in combination with several reflector materials; HT9 steel, 316 steel and natural Lead. Simulations of a natural Lead reflector were carried out in which the Lead was alone or encased in steel. For this study on reflector thickness, the radius and height of the active core were fixed at 225 cm and 450 cm, respectively. The results of this work is presented in section 5.1 and a summary table of optimum reflector thicknesses may be seen in 5.1.

4.4 DPA Calculations

A method for estimating the radiation damage in materials in the form of Displacements Per Atom (DPA) was adopted from a previous study by Staffan Qvist [65], who in turn used element-wise 100 energy-group cross-section data and a general methodology from the Argonne National Laboratory SPECTER code documentation [35]. A weighted sum of the cross section data obtained from the SPECTER code was used to produce a composite DPA cross section for HT9 steel which can be found in figure 4.3, with sample spectra from simulations of Reactor Geometry B with a 30 cm HT9 steel reflector included for reference.

For compound materials such as steel, we assume that each component element is distributed uniformly in the material, such that the probability that a primary recoil atom will collide with a particular type of matrix atom is only dependent on the atomic fraction of that type of matrix atom. This assumption that the material (i.e. HT9 steel) is homogeneous is necessary to estimate the damage in the material without prior knowledge of elemental segregation [33]. In addition to this assumption, for the calculation of displacement-energy (that is the energy of the primary knock-on atom or E_{PKA}), it is assumed that the contribution of each element can be added together, weighted by it's atomic fraction [35]. The general form of the DPA calculations are described in equation 4.1.

$$\text{DPA } s^{-1} = \sum_{j=1}^{N_{elements}} \left(\frac{0.8}{2E_{D,j}} * \frac{N_j}{N_{tot}} * \sum_{i=1}^{100} \sigma_{i,j} \phi_i \right) \quad (4.1)$$

where:

- $N_{elements}$ is the number of distinct elements in the composite material, e.g. steel.
- $E_{D,j}$ is the displacements energy in eV. This is the energy required to displace one atom of element j from the lattice.

- $\frac{N_j}{N_{tot}}$ is the atomic fraction of element j in the lattice.
- $\sigma_{i,j}$ is the displacement damage-energy cross section (keV-barn) for the i th energy bin and the j th element.
- ϕ_i is the neutron flux collected in the i th energy bin ($\text{n cm}^{-2} \text{s}^{-1}$).

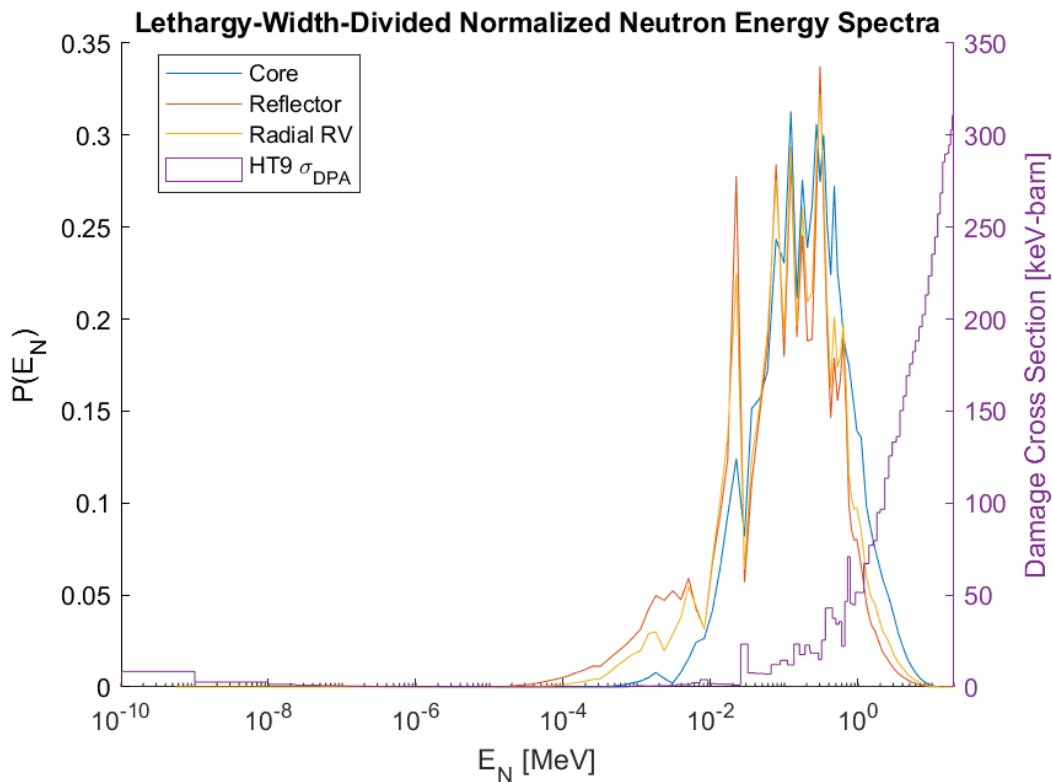


FIGURE 4.3: Neutron energy spectra and histogram of damage-cross section data for HT9, produced using the SPECTER code documentation [35].

4.4.1 DPA Model Benchmark

Efforts to benchmark this method of DPA estimation have been carried out previously by comparing measured radiation damage of open test assemblies from the Fast Flux Test Facility (FFTF) experiment and a 0-D simulation of the same reactor in MCNP [84]. In order to compare the code written in with that written previously and with experimental results, a table of measured fast fluences and the respective corresponding DPA values are tabulated in table 4.3.

The values of DPA-per-fast-fluence produced by each of the studies in table 4.3 range between 3.7 and 5 DPA / 10^{22} n, so one may tentatively conclude that the DPA model used in the present work appears to be valid. However, the lowest DPA-per-fluence rate in table 4.3 was produced by our model, which led to concerns that the radiation damage rate may have been

TABLE 4.3: Various DPA-per-fast-fluence results for validation of the DPA calculation method.

Source	$\phi_{>0.1 \text{ MeV}t}$ [n cm^{-2}]	DPA	DPA/ ϕt [$\text{DPA } 10^{-22} \text{ n}^{-1}$]	Material	Method
This Study	5.39×10^{23}	200	3.71	HT9	Blomqvist/SPECTER
[84]	10^{22}	4.0	4.0	HT9	Blomqvist/SPECTER
[74]	3.89×10^{23}	~ 155	4.1 - 4.5	HT9	Experiment
[43]	3.6×10^{23}	180	5	HT9	Experiment
[36]	1.00×10^{23}	43	4.30	Iron	Experiment

underestimated. All data listed in table 4.3 was obtained from computational or experimental studies of sodium-cooled fast reactors (SFRs), except for that of the present work. The authors of [84] were kind enough to provide neutron spectra and damage-cross-section data, to allow for comparison of the spectral differences between the MCFR and their SFR. The spectra of the MCFR core and the B&B SFR seed-region can be seen in figure 4.4. In addition, the neutron spectrum in the internal 5 cm of the MCFR HT9 reflector is plotted alongside the spectrum in the reflector region of the B&B SFR in figure 4.5.

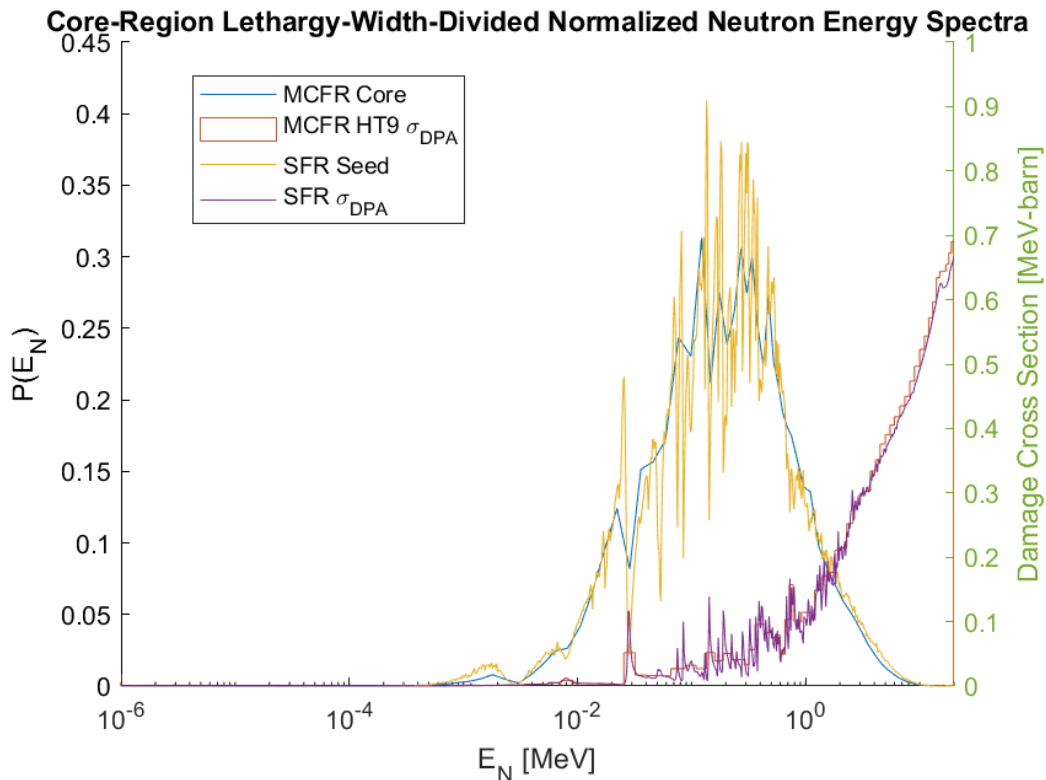


FIGURE 4.4: Neutron energy spectrum in the MCFR core. Histogram of damage-cross section data for HT9, produced using the SPECTER code documentation [35]. Seed-region SFR spectrum and SFR DPA cross section data provided by the authors of [84].

In these figures, the DPA cross-sections for the SFR study and this work are very similar, The same can be said when comparing the neutron energy

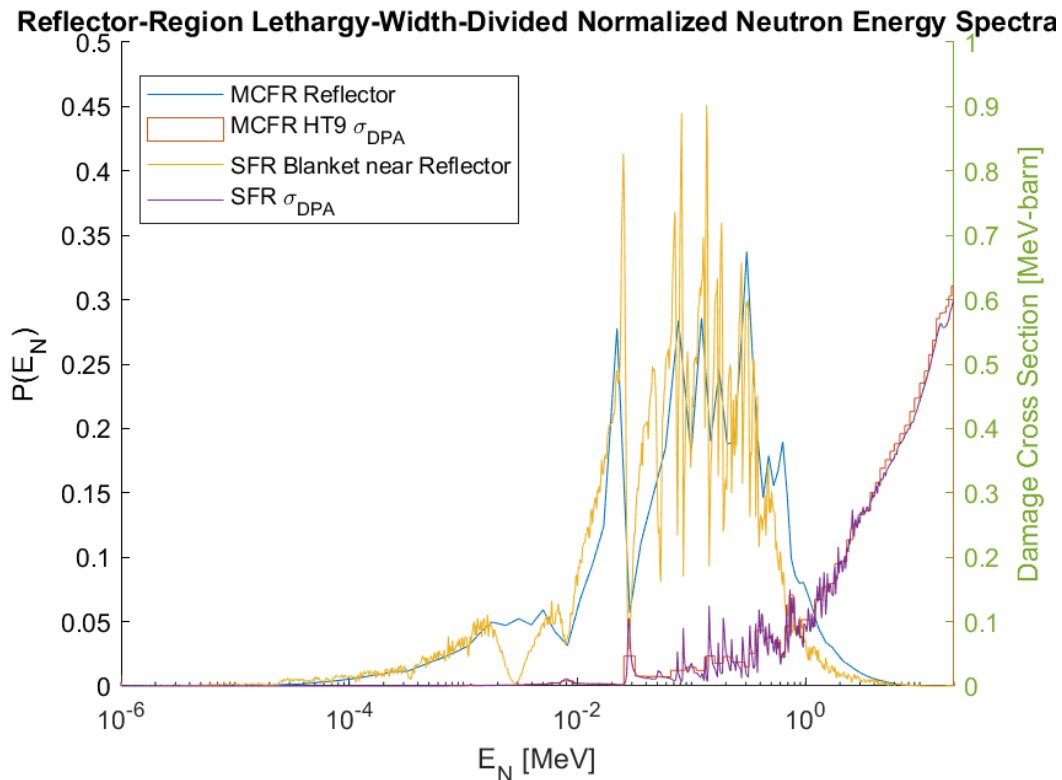


FIGURE 4.5: Neutron energy spectrum in the internal 5 cm of the MCFR reflector. Histogram of damage-cross section data for HT9, produced using the SPECTER code documentation [35]. reflector-region SFR spectrum and SFR DPA cross section data provided by the authors of [84].

spectra of the two studies. One would expect that for the same given fluence, both models would calculate similar values of DPA. Therefore, spectral differences and differences in DPA cross-sections can be ruled out as the source of the discrepancy in DPA-per-fast-fluence values in table 4.3.

It was also suspected that the difference in DPA-per-fast-fluence may have arisen for the different value for the displacement energy of HT9 steel (E_d) used in the SFR study. The authors of the SFR study chose 40 eV as a reasonable value for steels, as suggested in the literature [61]. In this work, displacement energies for the chemical constituents of HT9 steel were obtained from the SPECTER documentation (see table 4.2). However, when DPA calculations were re-run for the MCFR using $E_d=40$ eV, the results were almost entirely unchanged with a DPA-per-fast-fluence result of 3.69 DPA / 10^{22} n. Therefore it was concluded that the choice of E_d did not lead to the slight under-estimation of radiation damage accrual in comparison to the values produced by the previous SFR study.

While small, the origin of the disagreement between DPA models was not determined. The SFR spectra and cross sections in figures 4.4 and 4.5 were produced across a 1000-bin discretized energy grid ranging from 10^{-6} MeV

to 20 MeV. This was much finer than the 100-element energy grid ranging from 10^{-10} MeV to 20 MeV used in the present work. Although the two models appear similar, this difference in grid-size (by several orders of magnitude) may have led to the difference in results. However it should be noted that substantial fluence values were not observed at energies lower than 10^{-6} MeV, so differences in thermal and iso-thermal binning regimes are probably not a contributing factor the discrepancy between the two models.

4.5 Helium Production Calculation

Detectors were placed in the steel components in Serpent simulations of the MCFR Geometry B in order to obtain the flux values and the spectral-weighted 1-group cross sections necessary to solve equation 2.3. Solving this equation allowed the concentration of Helium atoms in the steel to be estimated, in atomic parts-per-million (appm). The results of these calculations, along with some validation efforts are provided in section 5.3.

As Helium builds up in crystalline materials such as steels, it segregates and accumulates along grain boundaries. This accumulation of Helium bubbles along grain boundaries is a primary cause of the life-limiting embrittlement of a material under irradiation. In a previous study on the build up of Helium in structural materials in the DEMONstration Power Station (DEMO) fusion reactor design, values for the critical concentration of Helium along grain boundary planes was estimated for several constituents of steel using density-functional-theory (DFT). By simplifying the migration process to grain boundaries, and assuming a small grain size of $0.5 \mu\text{m}$ for each of the body-centred-cubic (bcc) metals, the critical concentration along grain boundaries was used to obtain values for the critical bulk concentrations of Helium (in appm) for each of the transition metals studied [29] [59]. These values serve as an estimate of the Helium concentration necessary to substantially embrittle the steel. Therefore in the present work, these values were used to determine the in-core component lifetimes against Helium-induced embrittlement. Note that this Helium-embrittlement lifetime was calculated completely separately to the estimation of time necessary for components to reach 208 DPA in section 5.2 (the DPA lifetime).

4.6 Safety Calculations

As discussed in section 2.3, the only meaningful assessment of reactor safety that could be made in this study was the calculation of the temperature-reactivity coefficient and β_{eff} , because the study was limited to a neutronics simulation. Any meaningful simulation of a transient in the MCFR would require a multi-physics modeling approach, which was not feasible in the time-frame of this project.

The temperature-reactivity coefficient can be broken into sub-coefficients, as in equations 4.2 and 4.3 [57].

$$\alpha_{tot} = \alpha_{Doppler} + \alpha_{Dilation} \quad (4.2)$$

or equivalently,

$$\left(\frac{dk}{dT}\right)_{tot} = \alpha_{Doppler} + \alpha_{Dilation} = \left(\frac{dk}{dT}\right)_{Doppler} + \left(\frac{dk}{d\rho} \frac{d\rho}{dT}\right)_{Dilation} \quad (4.3)$$

where

- k is the criticality multiplication factor, interchangeable with k_{eff} for the finite geometries simulated in this study.
- T is the temperature of the salt in Kelvin.
- ρ is the density of the salt in g cm^{-3} , which changes as a function of temperature.
- $\alpha_{Doppler}$ and $\alpha_{Dilation}$ are the symbols of the Doppler reactivity coefficient and the salt dilation coefficient, respectively.

Note that ρ_0 , the initial density of the fuel salt, was pre-defined to be $3.54938 \text{ g cm}^{-3}$ because it was adopted from a previous MCFR study [58]. Therefore equation A.2 was re-arranged to produce equation 4.4, in order to obtain ρ_1 from ρ_0 . In all simulations which utilized this fuel composition, the equilibrium fuel density from the previous study was used for ρ_0 and equation 4.4 was used to obtain the perturbed density ρ_1 . While not strictly accurate, as our initial density value did not fulfill the condition $\rho_0 = a - bT_0$, the scaling relation produced reasonable results when applied to our pre-defined density value.

$$\rho_1 = \left(\frac{a - bT_1}{a - bT_0}\right) \rho_0 \quad (4.4)$$

It is also worth noting the means by which temperature was shifted in Serpent simulations. The Doppler coefficient was estimated by increasing broadening the neutron cross sections using the tmp argument when defining the fuel material in Serpent. The ENDF/B-VII.1 Evaluated Nuclear Data Library was used to obtain neutron cross sections for all nuclides simulated. This library provides cross section data at 300 Kelvin intervals, and the 900 Kelvin cross sections were consistently used in this study. The temperature increase was applied to this temperature, e.g. a ΔT of +100 K would be implemented by running two simulations, at 900 K (as provided by the ENDF library) and at 1000 K by applying the tmp argument in Serpent materials definition card.

In practice, α_{tot} can be evaluated by two methods. In the first method, the temperature increase is arbitrarily chosen and the change in fuel density is calculated to correspond to the temperature change. Both the temperature

and density of the fuel salt are then perturbed in the same Monte Carlo simulation to evaluate the effect on k_{eff} . For clarity, we shall call this method the *combined perturbation method*.

4.6.1 The Combined Perturbation Method

The combined method is perhaps more realistic, as it better reflects the simultaneous occurrence of the Doppler and dilation effects. Using this method, $\alpha_{tot,combined}$ is determined from the difference in k_{eff} as in equation 4.5.

$$\alpha_{tot,combined} = \frac{k_{T_1} - k_{T_0}}{T_1 - T_0} \quad (4.5)$$

However, as both temperature and density are changed simultaneously, the uncertainty calculated from the combined perturbation method can only take account of the uncertainties in k_{eff} arising from the Monte Carlo statistics, as shown in equation 4.6.

$$\delta\alpha_{tot,combined} = \frac{1}{T_1 - T_0} \sqrt{(\delta k_{T_1})^2 + (\delta k_{T_0})^2} \quad (4.6)$$

4.6.2 The Separate Perturbation Method

In the second method of evaluating α_{tot} the changes to temperature and density are calculated as in the combined method but $\alpha_{Doppler}$ and $\alpha_{Dilation}$ are determined from separate simulation runs. Then the two values obtained are added together to obtain α_{tot} in what we shall call the *separate perturbation method*.

When the temperature and density effects are simulated separately, as in the second method, the uncertainty associated with the engineering correlation used to determine the salt density from its temperature can be taken into account directly. Using the separate perturbation method, $\alpha_{tot,separate}$ is calculated using equation 4.7.

$$\alpha_{tot,separate} = \frac{k_{T_1} - k_{T_0}}{T_1 - T_0} + \frac{k_{\rho_1} - k_{\rho_0}}{\rho_1 - \rho_0} * (-b) \quad (4.7)$$

where b is a fitted constant from the density-temperature correlation in equation A.2. The densities obtained using this correlation are provided with an associated standard deviation. Hence by re-arranging equation A.2 and applying error laws as found in [78], we can obtain an uncertainty for the b parameter and, by extension, an uncertainty with our estimate of $\alpha_{tot,separate}$ as shown in equations 4.8 and 4.10.

$$\delta b = b \times \frac{\delta\rho}{\rho} \approx b \times \frac{\delta\rho}{\rho_{avg}} \quad (4.8)$$

where $\delta\rho$ is given in the engineering correlation as 0.003 g cm^{-3} [19] and ρ_{avg} is the average value of the density range for which the density correlation was said to be valid, as shown in equation 4.9.

$$\rho_{avg} = \frac{1}{2} * (\rho(T = 951K) + \rho(T = 1943K)) \quad (4.9)$$

$$\delta\alpha_{tot,separate} = \sqrt{(\delta\alpha_{Doppler})^2 + (\delta\alpha_{dilation})^2} \quad (4.10)$$

$$(4.11)$$

where $\delta\alpha_{Doppler}$ and $\delta\alpha_{dilation}$ are determined by equations 4.12 and 4.13, respectively.

$$\delta\alpha_{Doppler} = \frac{1}{T_1 - T_0} \sqrt{(\delta k_{T_1})^2 + (\delta k_{T_0})^2} \quad (4.12)$$

$$\delta\alpha_{dilation} = \frac{1}{\rho_1 - \rho_0} * |(k_{\rho_1} - k_{\rho_0}) * (-b)| \quad (4.13)$$

$$* \sqrt{\left(\frac{\sqrt{(\delta k_{\rho_1})^2 + (\delta k_{\rho_0})^2}}{k_{\rho_1} - k_{\rho_0}} \right)^2 + \left(-\frac{\delta\rho}{\rho_{avg}} \right)^2} \quad (4.14)$$

4.7 Burnup Calculations

As in the previous study on the B&B mode feasibility in the MCFR, a modified version of Serpent was used, which allowed the core composition to be gradually changed with different time constants specified for different nuclides [6]. As in [58], the feed-removal rate for gaseous fission products and noble metals was set to ensure an in-core half-life of 30 minutes. For all other isotopes, a range of 20 values of the feed-removal time constant were selected. These values were evenly spaced logarithmically between $7.51 \times 10^{-10} \text{ s}^{-1}$ and $2.69 \times 10^{-8} \text{ s}^{-1}$. These limits corresponded to average in-core half-lives of between approximately 29.3 years and 0.8 years.

In this context it is important to distinguish discharge burnup (as defined by the feed removal rate) and burnup days, which is the length of time simulated in the standard Serpent burnup simulations. For each combination of feed/removal rate and core radius, the simulation was run for 92,501 burnup days, equivalent to approximately 253.4 years to allow for the fuel composition to reach an equilibrium and for k_{eff} to converge to the equilibrium value. It is worth noting that in this work, there was no strict criteria for convergence imposed on k_{eff} to ensure it had become constant. However, the use of the long burnup time of 253.4 years ensured that k_{eff} was essentially unchanging by the end of each burnup run. This qualitative convergence can be seen in figure 5.10, which shows the evolution of k_{eff} for several feed/removal rates for a core radius of 230 cm.

Density [g cm⁻³]	3.48
Nuclide	Mass Fraction
U-238	5.17E-01
Pu-239	6.54E-02
Na-23	5.62E-02
Cl-37	3.62E-01

TABLE 4.4: Initial composition (by mass fraction) of the fuel used in burnup simulations in sections 5.5 and 5.6.

In all simulations the initial fuel composition consisted of NaCl-[Actinide]Cl₃%, in which the [Actinide]Cl₃% molecules had a molar ratio of 50 at. %. The total composition is provided in table 4.4. The mass density of this composition was obtained from the correlation described in appendix A.2, for a fuel temperature of 800°C. Chlorine was enriched to 100% in Cl-37. The Uranium-238 present was enriched to 11.2 % in Pu-239, as used previously [58].

Chapter 5

Results and Analysis

5.1 Radial Reflector Geometry

The following conditions apply to both Reactor Geometry A and B simulations which made use of a Lead reflector. A Lead reflector was simulated, both with and without a 5 cm thick HT9 steel casing. For the simulation using a 10 cm thick steel-encased Lead reflector, only the 10cm layer of steel casing was simulated. For steel-encased lead reflector simulations with a thickness ≥ 20 cm, the reflector consisted of 5 cm thick interior and exterior HT9 steel walls, with the remaining reflector volume being filled with natural Lead.

In the so-called pure-Lead simulations, the reflector walls and interior consisted entirely of natural Lead, without any steel casing. The pure-lead scenarios were simulated to represent the theoretically ideal reflector as a reference and preclude any parasitic absorptions in the steel casing. To clarify the difference between the steel-encased Lead and pure Lead, an image of radial cross sections of Reactor Geometry B in either scenario is provided in figure 5.1. In this image the natural Lead is brown and the HT9 steel casing is blue.

In the case of Reactor Geometry A, the reflector thickness was varied between 0 and 200 cm in 10 cm increments both **axially and radially**, in order to observe the combined effect of axial and radial reflection on criticality (see figure 5.2). In order to be consistent with the previous study using this geometry [58], pure 316 steel and pure HT9 steel were used as reflector materials. In addition, 90% steel/10% fuel-salt was simulated for both HT9 and 316, to allow for coolant channels in the reflector.

For Reactor Geometry B, the total thickness of the **radial** reflector was increased in 10 cm increments between 0 cm and 200 cm, as shown in figure 5.3. The influence on k_{eff} , leakage and fission rates was examined to determine the minimum thickness at which radial reflection had saturated for the given reflector material.

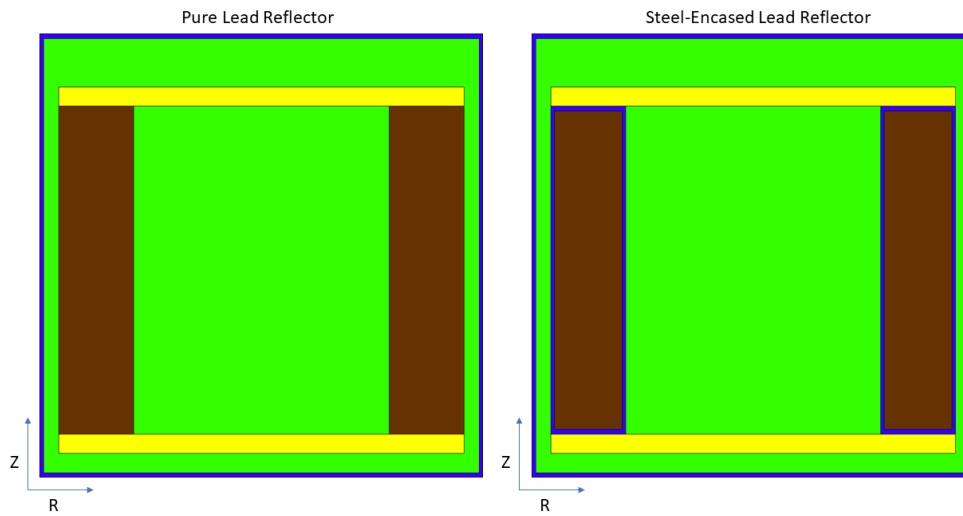


FIGURE 5.1: Radial profile of Reactor Geometry B using 100 cm pure Lead (left) and steel-encased Lead (right) reflectors.

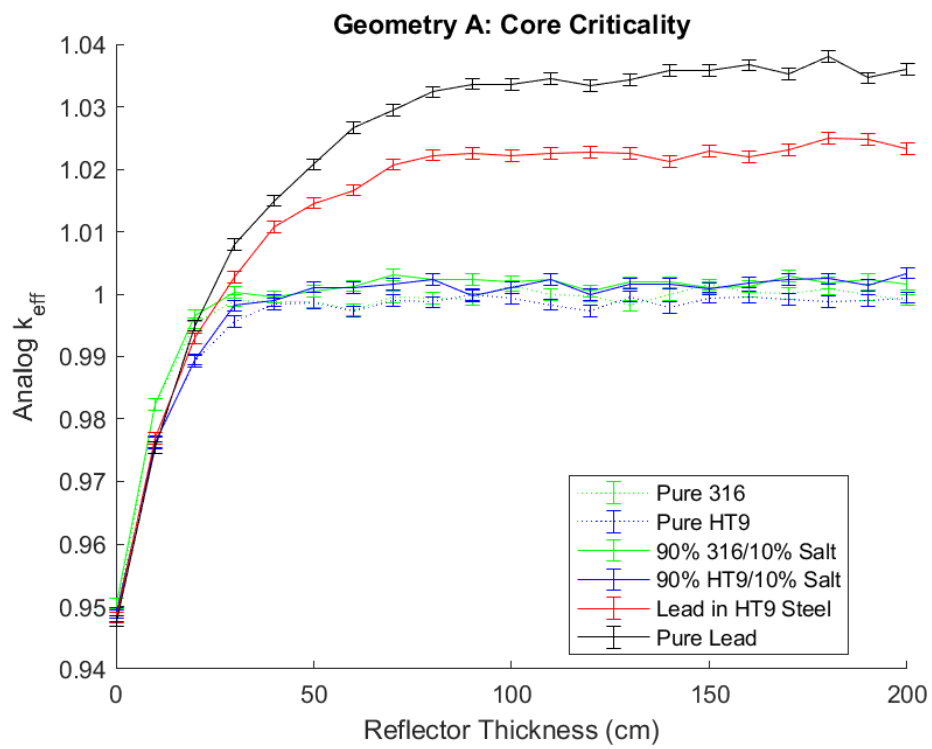


FIGURE 5.2: Criticality as a function of reflector thickness in geometry A.

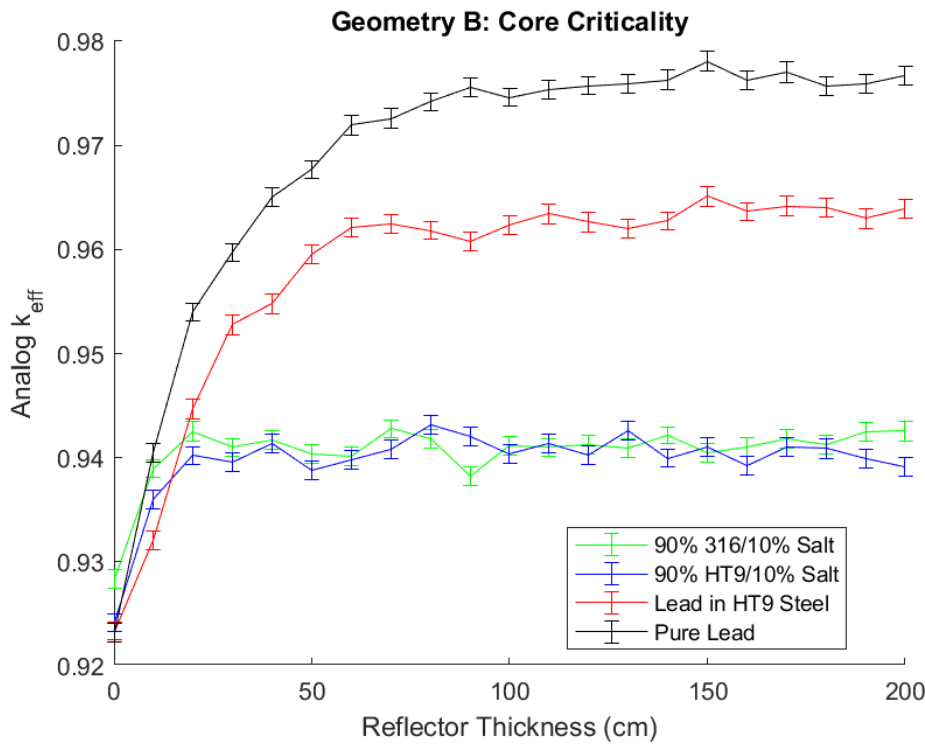


FIGURE 5.3: Criticality as a function of reflector thickness in geometry B.

5.1.1 Radial Reflector Simulation Results

Qualitatively, each trendline presented in figures 5.2 and 5.3 appears to monotonically increase with an exponential response before leveling off, presumably due to the saturation of the reflection effect. The equivalent reactivity insertion due to an increase in the thickness of the reflector can be observed to saturate for different thickness values, depending on the reflector material. However, for every reflector material simulated, the reactivity insertion has saturated prior to reaching 200 cm. Therefore, it is convenient for the purposes of this study to define the total-available-reactivity-worth of the reflector through the difference between the k_{eff} values of the reactor with a 200 cm reflector, and with no reflector present, which can be labeled k_2 and k_1 for convenience.

The difference between k_1 and k_2 was calculated, along with an associated uncertainty, using in equations 5.1 and 5.2. These were obtained by combining the uncertainty values for k_{eff} produced by Serpent, in combination with the error propagation laws outlined in [78]¹.

$$\Delta k_{eff} = k_2 - k_1 \quad (5.1)$$

$$\delta \Delta k_{eff} = \sqrt{(\delta k_1)^2 + (\delta k_2)^2} \quad (5.2)$$

¹Note: Although Serpent provides the relative uncertainty of results, only the absolute standard deviations are presented in the present work.

Reflector	d_{sat} [cm]	Δk_{eff} [pcm]	$\Delta k_{eff,200cm}$ [pcm]
Reactor Geometry A			
Pure 316	20	4685.7 ± 126.38	5057.2 ± 125.91
Pure HT9	30	4722.9 ± 129.86	5094.4 ± 125.9
90% 316/10% Salt	20	4608 ± 126.69	5108.5 ± 127.03
90% HT9/10% Salt	30	4913.9 ± 123.9	5431.3 ± 124.95
Lead in HT9 Steel	60	6838.5 ± 123.47	7502.5 ± 126.77
Pure Lead	70	8186 ± 128.53	8828 ± 126.72
Reactor Geometry B			
90% 316/10% Salt	20	1415.1 ± 127.76	1420.1 ± 128.45
90% HT9/10% Salt	20	1599.8 ± 122.64	1492.9 ± 123.24
Lead in HT9 Steel	60	3882 ± 122.74	4060.1 ± 120.08
Pure Lead	60	4871.3 ± 128.63	5349 ± 124.8

TABLE 5.1: Radial reflection saturation estimates for Reactor Geometries A and B.

Using equation 5.1, the reactivity insertion due to the addition of 200 cm of reflector for each of the curves plotting in figures 5.2 and 5.3 is provided, along with other quantities, in table 5.1. In this table, the saturation thickness d_{sat} was defined as the reflector thickness for which the increase in k_{eff} was 90% of the increase measured for the maximum reflector thickness of 200 cm. This criterion was defined in order to determine the minimum reflector thickness necessary to maximize the reflection of neutrons.

For an HT9 steel reflector in the Reactor Geometry B simulations, the reflection of neutrons was observed to saturate at approximately 20 cm in HT9 steel. This value of steel reflector thickness was concluded to be a good balance between neutronic and core-size concerns. This reflector materials composition and thickness was used in all further developments of the reactor model in the present work.

5.2 DPA Estimation / Component Lifetime Analysis

In this section, the lifetime of various core components will be estimated by determining the region of each component which most rapidly accrues radiation damage, in units of DPA-per-year, for full power operation at a total core power of 9.26 GWth, corresponding to an active-core fuel salt power density of 300 W cm^{-3} . In order to determine the spatial peak damage rate in a given component, the component will be divided into annular sections and the DPA-per-year rate determined by measurement of the neutron flux

in each section. In this way, we may take advantage of the cylindrical symmetry of the simulation to produce a 2-D map of DPA as a function of radial distance from the core center (r) and the axial height above or below the the core mid-plane (z). An example of such a color map, for a 20 cm reflector placed in Reactor Geometry B, is provided in figure 5.4.

This division of components into annular sections was achieved by use of cylindrical grid detectors placed inside each component of interest. In the linear-no-threshold NRT DPA model used in this study, the radiation damage accrued in a particular region is assumed to be linearly proportional to the neutron flux for a flux of fixed energy. Therefore, the granularity of the detector grid superimposed over each component in the r and z directions was chosen to be less than the mean free path for neutrons in HT9 steel. We reasoned that radiation damage effects would be roughly homogenized at finer granularities than the range of the neutron mean-free-path. This was estimated by measuring the total neutron cross section (for both absorption and scattering) as a function of radial depth into a 100 cm HT9 reflector, as shown in figure 5.5. The maximum cross-section in this plot corresponds to a minimum neutron mean free path of 2.44 cm. Therefore, the radial and axial detector grid lengths were chosen to be 1 cm to be able to resolve the peak DPA-per-year rate in HT9 components.

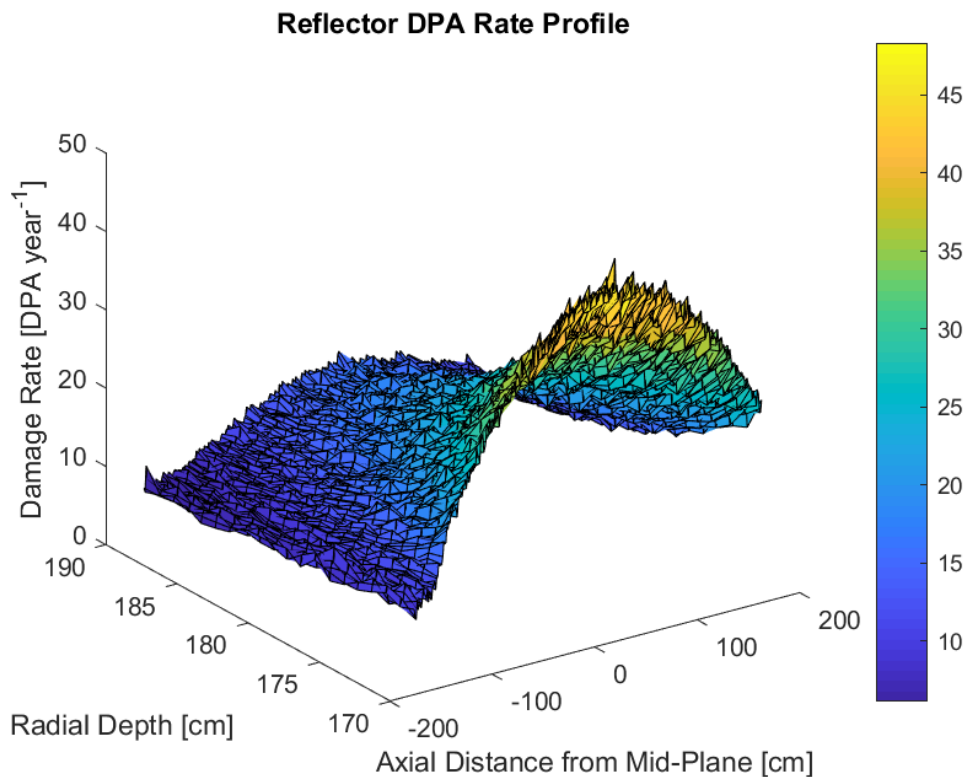


FIGURE 5.4: Radiation damage rate as a function of r and z position in the 20 cm 90% HT9/10% Salt reflector.

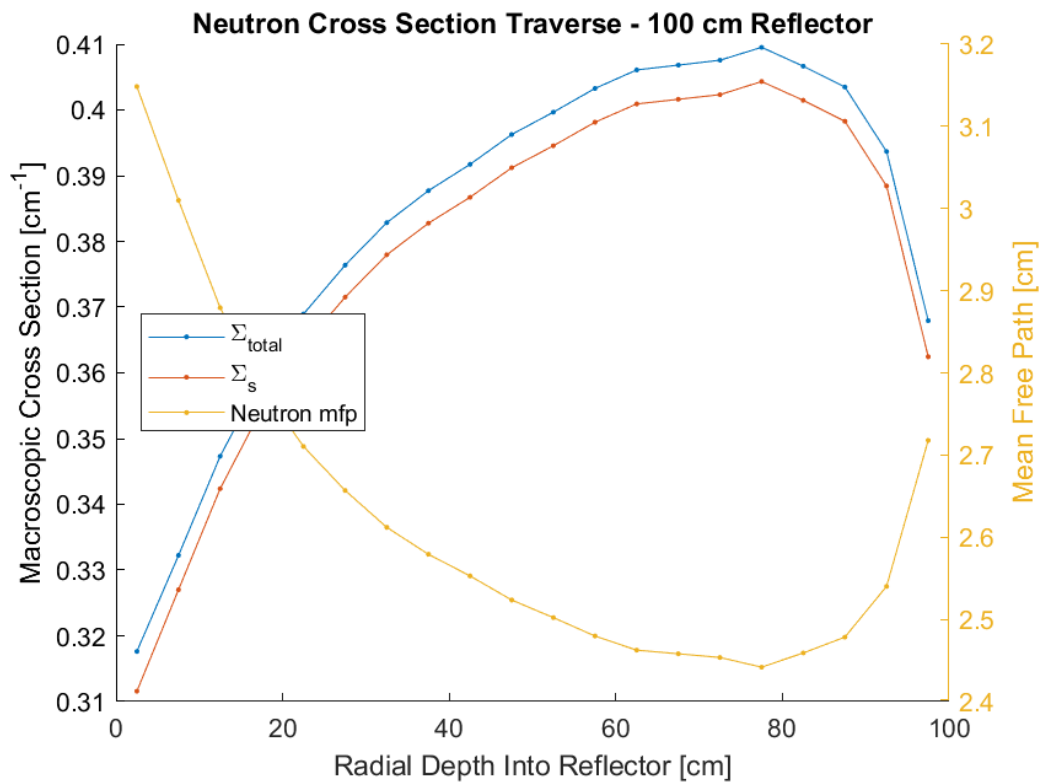


FIGURE 5.5: Macroscopic neutron cross-sections in a 90% HT9 / 10 % Fuel Salt reflector in Reactor Geometry B.

This methodology of dividing components into annular sections in which the DPA rate would be estimated was applied to each steel component in the Reactor Geometry B simulation with fixed reactor power of 9.26 GWth and a 20 cm reflector comprised of 90% HT9/10% Salt. The maximum DPA/year rate in a given component was used to estimate the component lifetime, corresponding to the 208 DPA limit commonly considered for HT9 steels. The initial results for each component are provided in table 5.2.

Component	Peak DPA/year	Axial Position [cm]	Radial Position [cm]	Lifetime [years]
Reflector	48	26.5	170.5	4
Upper Steel Internals	143	180.5	0.5	1
Lower Steel Internals	70	-177.5	1.5	3
Radial Reactor Vessel	9	10.5	210.5	24
Upper Reactor Vessel	34	242.5	0.5	6
Lower Reactor Vessel	22	-212.5	0.5	10

TABLE 5.2: Estimated component lifetimes, using a 208 DPA limit.

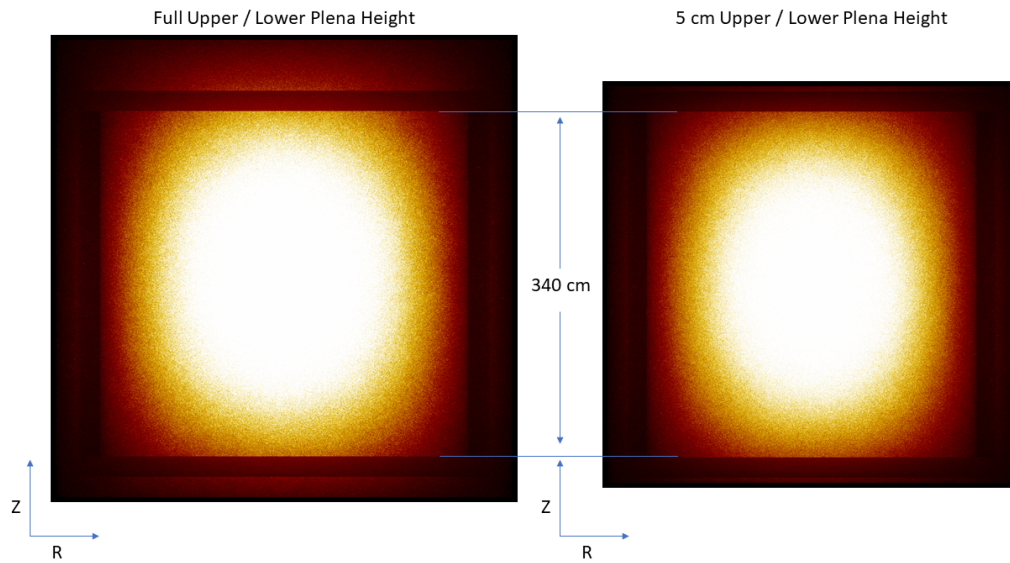


FIGURE 5.6: Radial cross sections of the power profile before and after the plena heights were reduced to 5 cm.

Component	Peak DPA/year	Axial Position [cm]	Radial Position [cm]	Lifetime [years]
Reflector	51	16.5	170.5	4
Upper Steel Internals	67	173.5	1.5	3
Lower Steel Internals	77	-179.5	0.5	3
Radial Reactor Vessel	9	13.5	210.5	24
Upper Reactor Vessel	18	196.5	6.5	11
Lower Reactor Vessel	24	-195.5	0.5	9

TABLE 5.3: Component lifetimes with plena heights reduced to 5 cm, using a 208 DPA limit.

5.2.1 Reduced Plena Volume Simulations

The shortest component lifetime estimates were for the upper and lower steel internals in the core, with the upper steel internals reaching 208 DPA after just one year. In a real reactor, these regions could consist of flow channels, pumps or heat exchangers. Clearly replacing such components every year would be unfeasible. Knowing this, the ex-core salt geometry was changed to reduce the volume of salt in the upper and lower plena. It was hoped that by reducing the volume of these fissile regions, the power profile would not extend so far axially up and down. The lower plenum height was reduced from 20 cm to 5 cm and the upper plenum height was reduced from 50 cm to 5 cm. All other geometric parameters were left unchanged. A comparison of the power profiles provided by the Serpent simulation is provided in figure 5.6. It can be seen that the neutron flux in the upper and lower steel internals was marginally reduced. The component lifetimes were re-calculated and the results are provided in table 5.3. With the upper plenum volume reduced, the estimated lifetime of the upper steel internals increased from 1

to 3 years. In addition, the lifetime of the upper reactor vessel increased from 6 to 11 years. It appears that by reducing the height of the plena to both equal 5 cm, the power profile became more axially compact and symmetric. However, having to replace the upper and lower steel internals after only 3 years is still unsatisfactory. Efforts to develop ferritic-martensitic steel which can withstand up to 600 DPA are underway by Terrapower for use in their TWR design [39]. However, this design challenge is common to all fast breeder reactor development; experimental irradiation data must be produced and analyzed in order for the standard damage constraint to be raised above ~ 200 DPA.

The influence of reducing the plena volumes on the criticality of the reactor was also examined. Using equations 5.1 and 5.2, the influence on k_{eff} is given in the expression below.

$$\Delta k_{eff} = k_{eff,5\text{ cm plena}} - k_{eff,normal} \quad (5.3)$$

$$= 0.932361 - 0.939239 \quad (5.4)$$

$$= -0.0069 \pm 0.00093 \quad (5.5)$$

$$= -690 \pm 93 \text{ pcm} \quad (5.6)$$

By reducing the volumes of the plena, we have negatively effected k_{eff} . However, this contribution to criticality primarily arose from ex-core fissions, which are problematic to begin with and should be avoided. If a large volume of salt is required in these regions, to ensure a certain flow velocity or hydraulic performance for example, then shielding should be used just outside of the upper and lower steel internals to minimize ex-core fissions. Placing such shielding inside of the steel internals would substantially improve the lifetime of these steel components, but would have a substantial negative effect on k_{eff} . Further studies will be required to determine the optimal combination of shielding, plena heights and reflectors.

5.3 Helium Production Results

5.3.1 Helium Build-Up Model Verification

The amount of Helium produced through neutron capture in nickel isotopes was determined using the method discussed in section 4.5. Helium production is often related to the rate of radiation damage in a material as quantified by DPA. A study conducted at Oak Ridge National Laboratory on Helium build-up in materials irradiated in the FFTF experiment found Helium to build up at a rate of 0.28 appm/dpa in Prime Candidate Alloy (PCA) steel [37].

It was hoped that the Helium build-up model used in this study could be partially validated by comparison with this result obtained for the FFTF. First it was necessary to compare the typical neutron spectra from the two reactors, as both radiation damage and Helium production are heavily spectrum-dependent. The neutron spectrum produced by a zero-dimensional model of

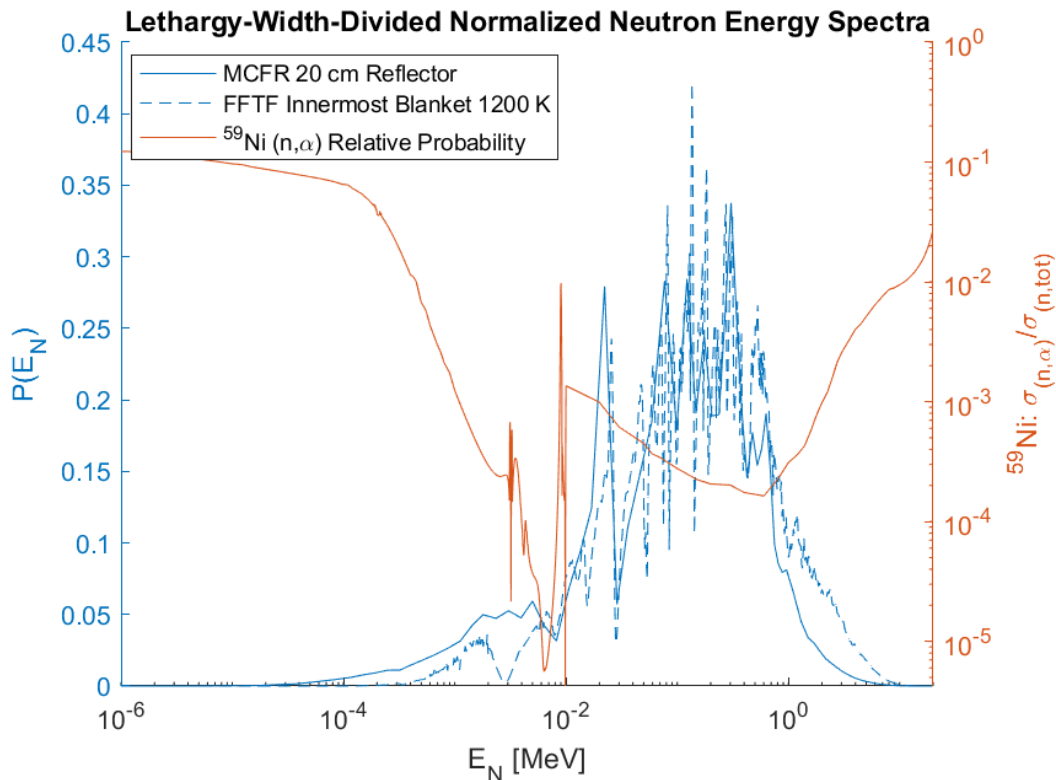


FIGURE 5.7: Neutron spectra in the 20-cm-thick 90% HT9 / 10 % Fuel Salt reflector in the MCFR and in the FFTF [84].

the innermost blanket in the FFTF was kindly provided by the authors of a previous study at UC Berkeley [84]. This FFTF spectrum is provided alongside the neutron spectrum inside the 20 cm MCFR reflector in figure 5.7. In addition to the neutron spectra, the relative probability of alpha emission in ^{59}Ni calculated from the ENDF/B-VII.1 cross section library was plotted. This relative probability was obtained through a ratio of microscopic cross sections, as defined in equation 5.7. The trend of this ratio provided in figure 5.7 illustrates the energy-dependence of Helium production by neutron capture in ^{59}Ni .

$$P_{\text{rel}}(n, \alpha) = \frac{\sigma(^{59}\text{Ni}(n, \alpha))}{\sigma(^{59}\text{Ni}(n, \text{tot}))} \quad (5.7)$$

As can be seen in the figure, the relative probability of Helium production in ^{59}Ni is highest in the thermal/epithermal region. The neutron spectra of the FFTF and MCFR were deemed to be sufficiently similar in this energy region to ensure that a comparison of the resultant DPA and Helium accrual rates seemed a reasonable way to partially validate the Helium build-up model.

By using the DPA calculation method described in section 4.4, it was possible to obtain a value for the Helium/dpa rate for HT9 steel used in the MCFR simulation. The radiation damage accrued after 1 year of fluence in the 20 cm reflector was 19.18 DPA. In the same period of time, the helium built up in the reflector reached ~ 0.69 appm. This equates to a Helium-per-DPA value of 0.0036 appm/dpa, which is approximately 1.3% of the value obtained for

the FFTF. The ratio of this values is given below.

$$\frac{\text{He-per-DPA}_{PCA}}{\text{He-per-DPA}_{HT9}} = \frac{0.28}{0.0036} \approx 77.78 \quad (5.8)$$

The PCA steel irradiated in the FFTF consisted of 15.5 at. % Nickel. In contrast the HT9 steel used in this study had a relatively low Nickel content of 0.47 at. %. The ratio of these two atomic fractions is given below.

$$\frac{N_{Ni}(PCA)}{N_{Ni}(HT9)} = \frac{15.5}{0.47} \approx 32.98 \quad (5.9)$$

Working under the assumption that the rate of Helium build-up is linearly proportional to the initial number density of Nickel-58 atoms, as predicted by equation 2.3, one would expect the ratios in equations 5.8 and 5.9 to be equal one another. While they differ by more than a factor of two, this discrepancy may be a result of differences in neutron spectra between the MCFR and the FFTF. In addition, the FFTF spectrum provided in figure 5.7 may not be representative of the neutron energies experienced by the PCA sample in which Helium build-up was measured. In order to better evaluate the Helium build-up model used in this study, it could be applied to a model of the FFTF and compared with the experimental results from [37]. However this was not completed in this study due to time constraints. For the purposes of this study, the order-of-magnitude agreement between equations 5.8 and 5.9 served as a partial validation of the Helium build-up model used, albeit with the caveats discussed below.

This means of validating the Helium build-up model relies on the DPA model discussed previously. Therefore this method of validation does not preclude the possibility of some systematic bias or error to which both the Helium and DPA models were subject. As a counterpoint, the DPA model used has been shown to be in general agreement with experimental data (see section 4.4), so any systematic error shared by both models is unlikely to be very large.

In addition, the simplified model outlined here does not account for Helium production due to neutron capture in nuclides other than ^{58}Ni , nor does it take account of Hydrogen build-up, another cause of steel embrittlement. For example, one study identified (n, α) reactions in Nitrogen, a common impurity in steels, as being a substantial source of Helium in EBR-irradiated Type-304 stainless steel. In addition, Nitrogen is known to migrate along temperature gradients in steels and may contribute to increasing peak Helium concentrations locally [21]. All of these phenomena should be considered in further modeling the effects of irradiation on structural materials.

5.3.2 HT9 Helium Production

As discussed in section 4.5, values for the maximum permissible Helium concentration in grains of the crystalline material were adopted from [59] and used to determine the lifetime-against-Helium-embrittlement in HT9 steel. Specifically, the value of 764.6 appm Helium in an Iron lattice was adopted as the critical embrittlement concentration. This value seemed the most appropriate as Iron is the dominant constituent in steels and this value was the smallest of the element-specific critical Helium concentrations provided by the study. For these reasons, the use of 764.4 appm as a Helium density limit was seen as both a reasonable and conservative choice for the estimation of Helium embrittlement in HT9 steel.

In modeling the build-up of Helium due to neutron capture in Nickel, it was observed that Helium appm values would saturate over very large time-scales. In figure 5.8, the concentration of Helium converges to a constant value of approximately 418.9 appm, substantially below the critical embrittlement limit for Iron of 764.4 appm. This occurs because, for very large values of t , equation 2.3 approaches the equation below.

$$\frac{N(\text{He})}{N_0(^{58}\text{Ni})} \approx \frac{\sigma_\alpha}{\sigma_T} \quad (5.10)$$

Hence, when the number density of ^{58}Ni and the 1-group cross-sections produced by Serpent are substituted into equation 2.3, the model from [34] predicts that Helium concentrations in the reflector will converge to approximately 418.9 appm. Note that this value is of course directly proportional to the initial concentration of ^{58}Ni in the steel. This fact serves as the main driver for selecting low-Nickel steels (such as HT9) for high-fluence applications, as shown elsewhere in the literature. While the component-averaged Helium concentrations seemed unlikely to reach the saturation value before reaching the limit defined by equation 5.10, it remained to be seen if peak Helium appm accrual rates in each component would reach this embrittlement constraint.

To determine the peak Helium appm levels, each component was divided into annular sections of radial and axial increments of 1 cm, in a similar approach to that taken for the peak DPA calculations. The Helium concentration profile in the radial reflector after 100 years is given in figure 5.9.

The maximum Helium appm in each component after 100 year of fluence (i.e. 100 full-power year at 9.26 GWth), along with its location, is provided in table 5.4. This time-frame seemed a good representation of the maximum reactor lifetime. As expected, the highest Helium concentrations occur in components directly in contact with the active core. For all of the 1 cm annular sections in all components, the maximal Helium concentrations saturated at values between 300 to 400 appm below the critical embrittlement concentration of 764.4 appm.

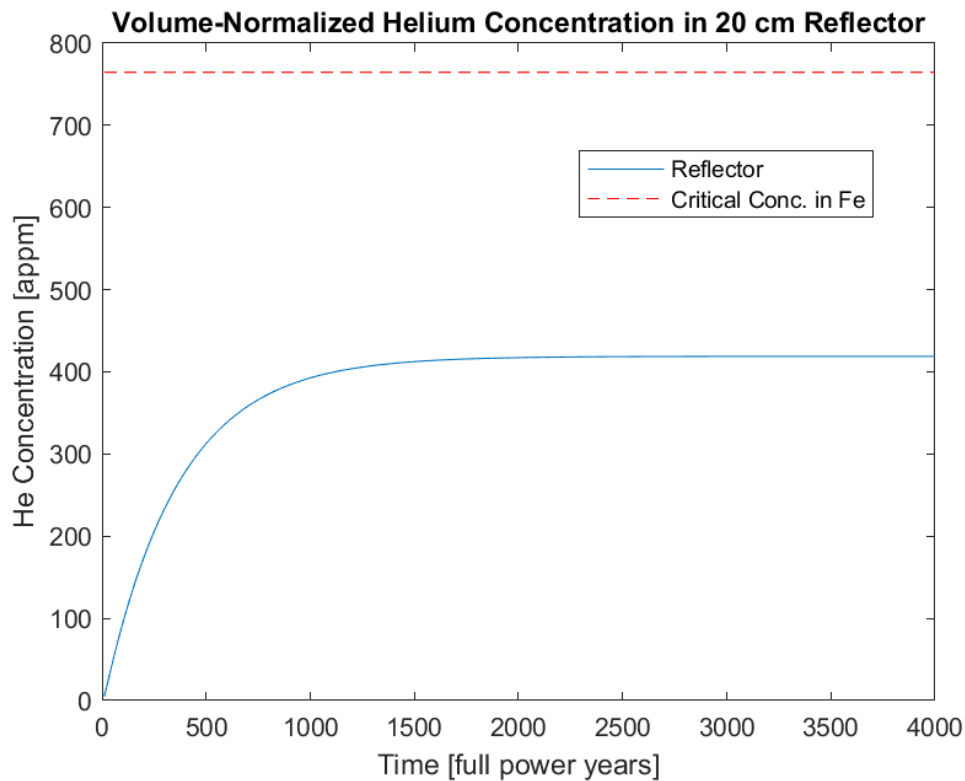


FIGURE 5.8: Average Helium build-up in the 90% HT9/10% Salt 20 cm reflector.

TABLE 5.4: Maximum Helium concentrations after 100 full-power years (FPY).

Component	Peak He appm	Axial Position [cm]	Radial Position [cm]
Reflector	144.2	7.5	171.5
Upper Steel Internals	143.5	183.5	2.5
Lower Steel Internals	70.9	-173.5	3.5
Radial Reactor Vessel	21.2	37.5	210.5
Upper Reactor Vessel	27.1	240.5	12.5
Lower Reactor Vessel	12.9	-210.5	10.5

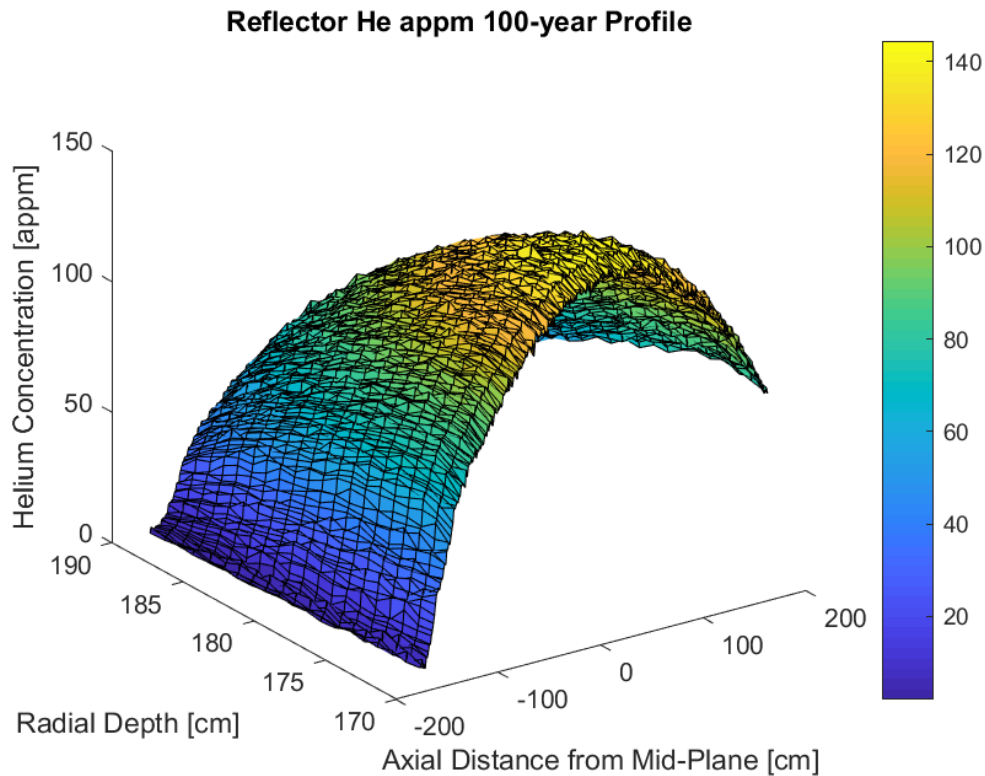


FIGURE 5.9: Helium concentration profile in the 90% HT9/10% Salt 20 cm reflector after 100 FPY.

Hence for the MCFR fluence and neutron spectrum in conjunction with HT9 steels, we can tentatively conclude that Helium production by neutron absorption in Nickel isotopes will not be the primary driver of component embrittlement and will not be the limiting factor in component lifetimes. However, the Helium concentrations reached over the reactor lifetimes are certainly non-negligible and should be taken into account in further studies. Tensile and Charpy tests conducted on HT9 and other steels irradiated in the FFTF and HFIR experiments have shown that Helium build-up through Ni-58 capture enhances the increase in the Ductile-to-Brittle Transition Temperature (Δ DBTT) and increased the sample hardness [50] [51]. However due to the low nickel content in HT9 steel, the irradiation limit of 208 DPA was maintained as the primary factor in determining component lifetimes for the rest of this study.

5.4 Reactivity Coefficient Results

The methods to determine the temperature-reactivity coefficient, α_{tot} , discussed in section 4.6 were applied to the Reactor Geometry B MCFR design, using a 20 cm thick, 90% HT9/10% Salt radial reflector. The fuel used was the equilibrium composition of the 50 at.% [Actinide] Cl_3 chloride salt obtained through long burnup simulations at a constant feed/removal rate in a finite steel-reflected cylinder (i.e. Reactor Geometry A, see figure 4.1), as discussed

$\alpha_{tot,combined}$	-3.9900 ± 12.6201	-9.3000 ± 2.5857	-6.3190 ± 1.2713	-7.3140 ± 0.6361
$\alpha_{Doppler}$	-9.8700 ± 12.9554	-3.0980 ± 2.5494	-1.2800 ± 1.2817	0.5090 ± 0.6349
$\alpha_{Dilation}$	-28.0348 ± 12.9009	-7.3617 ± 2.5676	-8.0921 ± 1.2944	-7.3308 ± 0.6218
$\alpha_{tot,separate}$	-37.9048 ± 18.2832	-10.4597 ± 3.6183	-9.3721 ± 1.8216	-6.8218 ± 0.8886

TABLE 5.5: Temperature-Reactivity coefficients obtained using the combined and separate perturbation methods in units of pcm K⁻¹.

in 3.1 and kindly provided by the authors of [58].

Values of the temperature-reactivity coefficient calculated by the combined and separate methods for four different temperature increase values are provided in table 5.5.

The accuracy of the α_{tot} estimates was determined primarily by the relative error in measurements of k_{eff} . This effect can be seen in the large uncertainties associated with α_{tot} estimates for the smallest temperature perturbation of +10 Kelvin. In these measurements, the difference between the perturbed and un-perturbed k_{eff} values was sufficiently small to allow for the statistical uncertainty associated with both values (produced as a result of the Monte Carlo simulations) to become significant. Therefore, the α_{tot} results associated with the +10 Kelvin temperature perturbation may be ignored.

With the exception of the +10 Kelvin perturbation values, the values of α_{tot} produced by the combined and separate perturbation methods are in good agreement.

By taking an average of these values (excluding the +10 Kelvin results), weighted by the inverse square of their associated uncertainties, we may obtain a final estimate of α_{tot} , as in equation 5.11.

$$\alpha_{tot,avg} = \frac{\sum w_i \alpha_{tot,i}}{\sum w_i} \quad (5.11)$$

where $\alpha_{tot,i}$ is the i th estimate of the the temperature-reactivity coefficient and w_i is the weight associated with it, defined in equation 5.12.

$$w_i = \frac{1}{\delta_i^2} \quad (5.12)$$

The uncertainty associated with the final value is given in equation 5.13.

$$\delta_{\alpha_{tot,avg}} = \frac{1}{\sqrt{\sum w_i}} \quad (5.13)$$

Using these equations, the weighted average value of the temperature reactivity coefficient in the temperature perturbation range of +50 to +200 Kelvin was calculated to be -7.2973 ± 0.4525 pcm K⁻¹. This strongly negative value should ensure the safety of the core during a transient overheating event and represents a very desirable inherent safety feature. However this optimistic neutronic result says nothing of the finer details of the response of MSRs

to transient events, which are driven by the complex neutronic/thermal-hydraulic/thermo-mechanical feedbacks. For these scenarios to be truly understood, mature multi-physics models must be developed and validated against experiment.

5.5 Discharge Burnup & Minimal Core Dimensions

The core volume and feed/removal rate are the main factors in determining criticality, the nuclide inventory and the fissile-to-fertile ratio in the core. In order to determine the minimum active core volume necessary to sustain the B&B mode, burnup simulations were run for a range of feed/removal rates of fertile material into the fuel and core radii. The goal was to determine the behavior of k_{eff} as a function of these two parameters and plot the results.

The core geometry selected for study was the reduced-plena version of Reactor Geometry B (see figure 4.2, introduced in section 5.2.1). For each simulation, the core height was set to twice the core radius, maintaining a height to diameter ratio of one. The axial and radial thicknesses of each section (i.e. the downcomer, upper and lower steel internals, UP, LP, and the reactor vessel) were held constant. Hence these component regions were simply shifted outwards as the core radius increased. The core power was modified to maintain a power density of 300 W cm^{-3} in the active core region as the core volume increased.

Bearing in mind the distinction between discharge burnup and burnup-days, it is important to understand that plotting the so-called equilibrium k_{eff} as a function of discharge burnup does not illustrate the evolution of criticality during start-up or in the approach to steady state. Instead it is a measure of converged criticality for the equilibrium fuel composition reached after long reactor run-times for a specific feed/removal rate and discharge burnup. Primarily, it serves as a measure of the criticality of the reactor at steady state, after several years of operation.

Burnup simulations were run to reach 92,501 full-power days, while the feed-removal rate was held constant. During this time, the feed material (natural uranium) gradually replaced the fission products and actinides in the core. The final value of k_{eff} obtained in these long burnup runs was considered to be the steady state value for the given value of τ and the corresponding fuel composition was taken to be the equilibrium composition. See figure 5.10 for an example of the evolution of k_{eff} with burnup-days. The log-time scaling of the axis was used to illustrate the trend in k_{eff} but note that on a linear scale, the k_{eff} values were essentially constant by the end of each burnup run.

The equilibrium values of k_{eff} are provided as a function of core radius and discharge burnup (in FIMA) in figure 5.11. The parameter space in which the breed and burn mode is feasible is determined, in essence, by the region in which the surface is greater than one. Some points of interest in the data

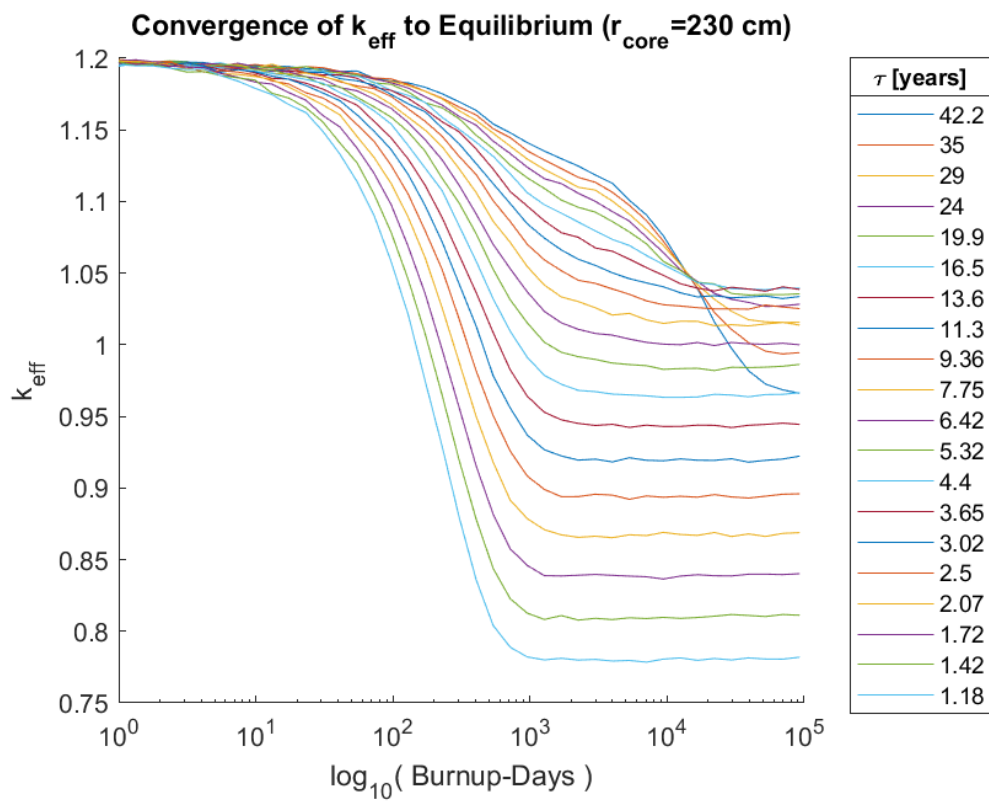


FIGURE 5.10: The convergence to the equilibrium composition k_{eff} for various fuel-in-core residence times in the 230 cm radius core.

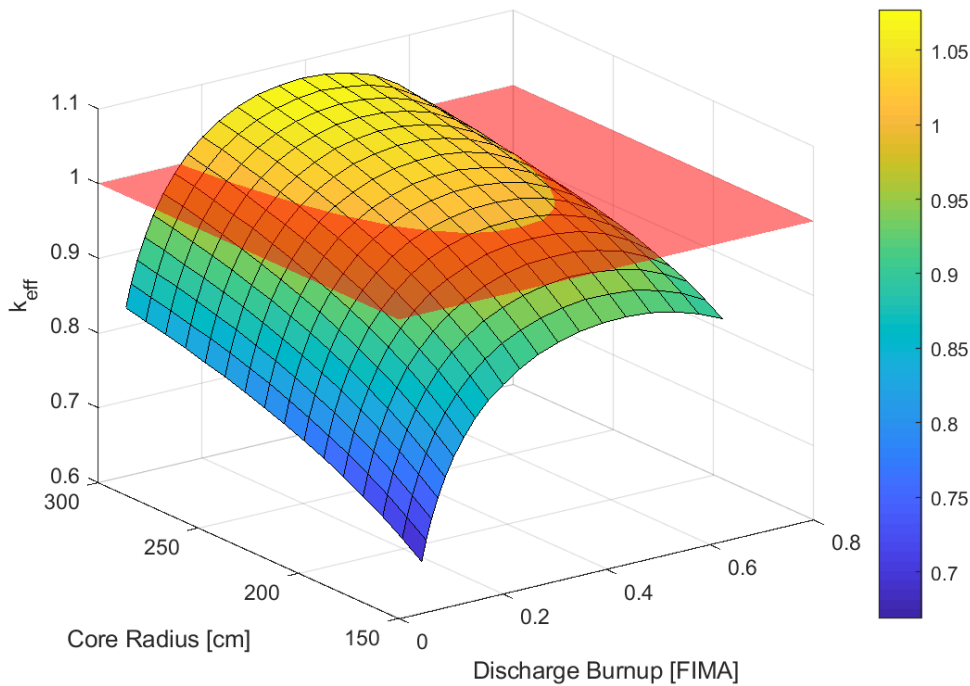


FIGURE 5.11: Equilibrium k_{eff} for Various Core Radii and Discharge Burnups. Criticality ($k_{eff} = 1$) indicated by the semi-transparent red plane.

are presented in table 5.6.

In the work preceding this study, the minimum core radius for steel-reflected B&B was identified as 225 cm [58]. In the current work the minimum radius estimate was reduced, at 200 cm. This may be due to the fact that while the *active* core volumes are the same in both studies, Reactor Geometry B had a significant volume of ex-core salt, which added to the overall nuclide inventory, allowing for a greater amount of fissile material in the simulation. Also the initial fuel salt mass density used in this study was 3.48 g cm^{-3} where as for the previous study it was set to 3.11 g cm^{-3} . This modest increase in density would increase the fissile and fertile densities in the simulation and may have allowed for criticality to be achieved at a slightly reduced volume.

The active core volume, total salt volume and the thermal power of each simulation displayed in figure 5.11 is provided in Appendix B. As multi-physics simulations were not conducted in this study, the influence of DNP drift (discussed briefly in section 2.3) could not be taken into account, which would reduce the realistic value of k_{eff} somewhat. Ex-core shielding was not included in the simulation, which could also have a small negative impact on criticality. The incompleteness of the model used, in considering only neutronics, means that one should adopt these minimum-core-volume estimates with caution.

It should also be noted that, as the composition of mixed materials (as

	k_{eff}	FIMA	τ [years]	r_{core} [cm]	α_{temp} [pcm/K]	β_{eff} [pcm]
Max k_{eff}	1.0766 ± 0.0003	0.3914	13.6381	300	-3.7 ± 0.2	349.216 ± 1.30
Min FIMA ($k_{eff} > 1$)	1.0000 ± 0.0003	0.1702	4.40	280	-4.3 ± 0.2	368.053 ± 1.51
Max FIMA ($k_{eff} > 1$)	1.0124 ± 0.0003	0.6226	35.00	300	-2.8 ± 0.2	334.467 ± 1.37
Min Radius ($k_{eff} > 1$, FIMA = min)	1.0032 ± 0.0003	0.3702	13.64	200	-5.9 ± 0.2	348.626 ± 1.35
Min Radius ($k_{eff} > 1$, FIMA = max)	1.0027 ± 0.0003	0.4614	19.88	200	-5.7 ± 0.2	359.578 ± 1.33
Min α_{temp} ($k_{eff} > 1$)	1.0121 ± 0.0003	0.2925	9.36	220	-6.1 ± 0.2	359.062 ± 1.41
Max α_{temp} ($k_{eff} > 1$)	1.0124 ± 0.0003	0.6226	35.00	300	-2.8 ± 0.2	334.467 ± 1.37

TABLE 5.6: Extrema of the critical k_{eff} surface in figure 5.11 and the α_{temp} surface in figure 5.12.

defined by the Serpent mix card) cannot be subjected to burnup calculations, the composition of the mixed steel/salt regions in the reflector and steel internals above and below the core were held constant. They were mixed manually by volume fraction, consisting of the initial fuel composition (defined in table 4.4) and the HT9 steel defined in table 4.2. Hence the influence of the changing composition of fuel salt in mixed steel/salt regions was not simulated and could not be taken into account. However, the use of the initial fuel composition in these mixed regions seemed to be an appropriate approximation.

5.6 Discharge Burnup and Reactor Safety

The temperature-reactivity coefficient of the reactor was evaluated for the equilibrium fuel compositions produced in the previous section. The separate and combined perturbation methods for evaluating the temperature reactivity coefficient in section 4.6 were shown to be in good agreement, with similar associated uncertainties (see table 5.5 for a comparison). Hence for the sake of computational simplicity, only the combined perturbation method was used for the various equilibrium fuel compositions produced in section 5.5. The temperature reactivity coefficient is plotted as a surface across the combined parameter space of core radius and discharge burnup (in FIMA) in figure 5.12. The temperature perturbation used in estimating α_{temp} was +200 Kelvin. The α_{temp} surface data was combined with data from the k_{eff} surface in figure 5.11 to produce table 5.6, which highlights various points of interest, such as the smallest critical core radius.

The combination of a core radius of 220 cm and an average in-core lifetime of 9.36 years produced the most strongly negative value of the temperature reactivity coefficient for all of the systems which were critical, at -6.1 pcm/K. The combination of a core radius of 200 cm and a in-core lifetime of 19.88 produced the highest achievable burnup (of 46.14% FIMA) for the smallest critical core volume. This configuration also had a large negative temperature

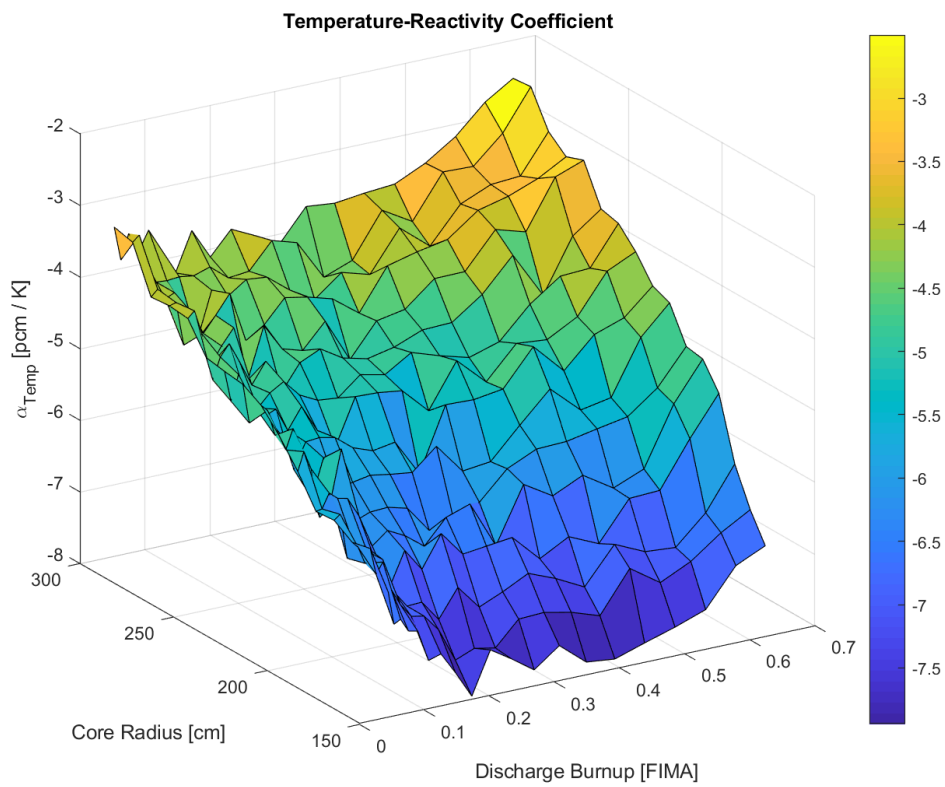


FIGURE 5.12: The temperature reactivity coefficient for the equilibrium fuel compositions discussed in section 5.5.

reactivity coefficient of -5.7 pcm /K. When one prioritizes the design goals of minimizing the volume of salt in the system while maximizing safety, then a core radius of approximately 210 cm may represent the optimum of all the systems simulated. However it remains a relatively large core, with the total volume of fuel salt (excluding mixed-salt regions) of 74 m³ and a power of $\simeq 17.46$ GWth, assuming a power density of 300 W cm⁻³ in the active core region. By using a lead reflector the core volume could be reduced, the advantages and drawbacks of which are discussed below.

5.6.1 Lead-208 Safety Benefits

Early in this study, the use of lead as a reflector material was rejected as a design decision due to its high density and the material challenges in containing liquid lead in steel inside the radial reflector. Such steel walls would have to withstand two distinct molten metals on the interior and exterior interfaces, one of which (lead) is known to be highly corrosive. However, it was clear in the early simulations which utilized a lead reflector that it provided superior neutron reflection to steel and would allow for smaller core volumes (see figures 5.2, 5.3 and the papers [58] and [41]). This effect is even more pronounced for the use of Pb-208, which has an extremely low cross section for neutron capture in addition to a high scattering cross section and large atomic mass. Hence it does not substantially thermalize neutrons and may be considered the optimal reflector material for fast reactors from a pure neutronics perspective.

With a large Pb-208 reflector, these properties may also serve to slow and mitigate the power increase during transient events in fast reactors. A recent study using a multi-point kinetics model of the lead-cooled BREST reactor design showed that by allowing a substantial fraction of fast neutrons to penetrate deep into the reflector before being reflected back into the core, the importance of prompt neutrons is substantially reduced. The fraction of neutrons leaking into the reflector may be larger than the effective delayed neutron, constituting a significant population of neutrons. This means that a substantial contribution to criticality (in the form of reflected neutrons) enters the core with a delay whose length may range between the prompt and delayed neutron lifetimes. In a transient scenario involving an instantaneous insertion of reactivity equal to $0.5*\beta$, the use of a Pb-208 reflector was shown to delay the power increase and decrease its magnitude [52].

In figure 5.12 the values of the temperature reactivity coefficient were all negative. However, in the case of an instantaneous insertion of reactivity into the MCFR core, the power would certainly increase before the salt dilation (and other negative thermal feedbacks) could come into effect. The rate of response to reactivity insertion, and the time-frame of a transient event, are determined in part by the effective delayed neutron fraction, β_{eff} . The

estimates of β_{eff} provided in table 5.6 were produced by Serpent and therefore do not account for DNP drift. Qualitatively, it can be seen that as the β_{eff} estimates are ~ 3 orders of magnitude less than those typically found for thermal reactors, transient events will take place much faster in this fast system. Therefore, reactivity control systems must be optimized to manage these faster transient events.

Much effort has been made to model the effect of DNP drift in MSRs. One study carried out various multi-physics models of a ^{233}U -started MSFR model with a total $\text{LiF-ThF}_4\text{-}^{233}\text{UF}_4$ fuel salt volume of 18 m^3 to observe the effect of fluid fuel circulation on β_{eff} . By using fluid dynamics models, the authors applied an importance function to neutron precursors based on their position in the core. This study estimated β_{eff} to be in the range of 700 to 300 pcm, for recirculation times ranging from 100 to 2 seconds [7]. We have taken this to imply that although no multi-physics models were carried out in this study, the values of β_{eff} provided in table 5.6 may still be used as a rough estimate.

Therefore, if future multi-physics studies of reactor transients should find the short-term power increase in fuel salts to be unacceptably high, then the safety benefits of Pb-208 may outweigh the materials and operational challenges inherent to working with liquid lead. The authors of this study also point out that, as Pb-208 lies at the end of the Th-232 decay chain, it can be extracted in high isotopic purity from the tails of some Thorium mines without the need of costly isotopic separation [76] [30].

Chapter 6

Discussion and Conclusions

Various geometry changes were made to Reactor Geometry B over the course of this study. The addition of a radial reflector had the greatest impact on criticality, which was to be expected. A 20 cm HT9 steel reflector increased k_{eff} by 1415.1 ± 127.76 pcm. When the reflector was changed to consist of natural lead encased in 5 cm of HT9 steel, the neutronic impact saturated at 3882 ± 122.74 for a 60 cm reflector thickness. By using a lead with a higher atomic fraction of Pb-208, the neutronic impact might be increased even more. As a suggestion for future work, it would be desirable to use a lead composition with higher Pb-208 (as much as is available in Thorium deposits) to evaluate to what extent the minimum core volume could be further reduced. Axial reflectors were not added in this study, but they could be also considered in future work to reduce the active core volume as much as possible.

In terms of practicality, the most limiting constraints found in this study arose from radiation damage effects. The upper and lower steel internals were found to have lifetimes of approximately 3 years, which seems infeasible from an operational and economic perspective. This problem is further complicated by the neutronic importance of these regions – this steel serves to reflect neutrons back into the core region. For example, reducing the plena volumes directly outside of the steel internals was observed to reduce k_{eff} by 690 ± 93 pcm. This change was $\sim 49\%$ of the increase in k_{eff} observed with the addition of the 20 cm steel radial reflector, so it is by no means insubstantial. Some potential avenues for reducing the fluence experienced by core components, without affecting criticality, are discussed below.

Placing shielding (such as boron carbide) between the steel internals and the active core would have a significant negative neutronic impact, and further reduce the space of equilibrium criticality (see figure 5.11). One possible strategy would be to place a sacrificial reflector material on the innermost layer of the steel internals and reflector. This could protect the flow channels and other components, while maintaining or even enhancing the reflection of neutrons back into the core. A similar strategy could be used to increase the projected lifetime of the radial reflector, currently estimated to be 4 years. Such sacrificial material would probably compose of a steel with a low neutron capture cross section and good performance at high temperatures. Of course, if radiation-resistance steels can be developed and qualified above 200 DPA, the projected lifetimes of all reaction components would increase

proportionally. Due to time constraints, radiation damage calculations (including the estimation Helium production) were only conducted for the 170 cm radius core using a 20 cm reflector. For larger cores with a proportionally higher thermal power, it is reasonable to expect the neutron fluence to be higher and the component lifetime estimates to be proportionally shortened, assuming the neutron energy spectra are similar for different core volumes. In future work, it would be desirable to re-apply the radiation damage calculations outlined here for the critical core volumes identified in section 5.5 and discussed below.

For low-Nickel content steels such as the HT9 used in this study, Helium embrittlement appears to have less of an impact on component lifetimes than DPA build-up. Indeed, according to the model used in this study, the low Nickel content causes the Helium concentration to saturate before the critical Helium concentration is reached. Other Helium production mechanisms, such as the (n, α) reaction in Nitrogen [21], should be evaluated to better understand the production of Helium in steel components, but for the purposes of this study, Helium production was deemed to be a less important radiation damage mechanism than the accrual of DPA.

Early on in this study, the decision was made to calculate material densities under the assumption of an operating temperature of 800 ° C, or 1073.15 K. While possible, this temperature is at the higher end of possible operating temperatures for the MCFR. A ternary phase diagram for the NaCl-UCl₃-PuCl₃ system suggests that the lowest melting temperature of 722 K or 448.85 ° C occurs for a molar ratio of of molar ratio (0.594-0.045-0.360) [10]. Although this composition has a molar fraction of [Actinide]Cl₃ lower than 50% and hence a lower melt temperature than the composition examined in this study, it seems that the operating temperature of the MCFR could be reasonably assumed to be lower than 800 C. Note that cross-section libraries were not subject to this poorly estimated operating temperature issue, as the temperature used in the acquisition of this data was always 900 K or 626.85 C. Specifically, this issue influenced the mass density calculations of steels, lead and the initial fuel salt used in burnup calculations for sections 5.5 and 5.6, outlined in table 4.4. While not a large source of error, this temperature/density issue is worth noting if one wishes to apply the results in this study to other reactor designs, particularly at lower operating temperatures where the fuel salt will be slightly denser.

The challenge of finding a steel which is qualified for full service life in a highly corrosive, high neutron flux environment up to high temperatures of between 700 and 800 ° C is a major one. Hastelloy-N was used successfully in FliBe salt for the entire duration of the MSRE experiment, but with a maximum service temperature of 977 K and a Nickel content of 68%, it would not be appropriate here for reasons of Helium embrittlement and operating temperature [68]. Oxide Dispersion Strengthened (ODS) steels show promise in having high strength at 1273 K and good resistance to radiation damage.

However the manufacturing techniques have yet to be scaled up for industrial purposes. Composite ceramics of of combined matrix / fiber phase, such as Silicon Carbide in the form of SiC/SiC, demonstrate excellent performance in corrosive, high-temperature and high-radiation environments, maintaining good mechanical strength up to 1375 K [83]. In the aftermath of the Fukushima Daiichi accident, much work has been done in the field of accident-tolerant fuels and cladding materials in the USA, and effort is underway to include SiC/SiC and other advanced materials such as Inconel Alloy 617 in the American Society of Mechanical Engineers (ASME) Boiler Pressure Vessel Code (BPVC) Section III, which the Nuclear Regulatory Commission (NRC) uses to qualify the permissible operating temperature for materials in nuclear applications [46] [5]. However with a Nickel content $\geq 44.5\%$, Inconel 617 is only intended for use in heat-exchangers and pumps in advanced reactors [18] [77]. Perhaps with the testing and qualification of new materials to high temperatures, the operating temperature of the MCFR can be raised to 800 ° C to avail of the higher thermodynamic efficiency and efficient Hydrogen production capabilities. In regards to SiC/SiC , it's efficacy as a neutron reflector remains to be seen, and steels or other materials may remain necessary for this purpose. Indeed, it could be worthwhile in future work to examine the neutronic impact of a SiC/SiC radial reflector or the combination Pb-208 encased in SiC/SiC.

The weighted-mean average value for the temperature reactivity coefficient was calculated to be -7.2973 ± 0.4525 pcm K^{-1} using the equilibrium fuel composition obtained from the previous B&B MCFR study. However this value was obtained for the 170 cm core radius, which was sub-critical using a steel reflector. The reactivity coefficient was evaluated for a range of core radii and discharge burnups, and for the critical simulations in which the core radius was minimized, the temperature-reactivity coefficient was between -6.1 ± 0.2 and -2.8 ± 0.2 pcm K^{-1} . The highest value of the α_{temp} was achieved for a core of radius 300 cm, the largest simulated, and a very high discharge burnup of $\sim 62\%$. This is likely due to the fact that at high burnups, the molar fraction of Plutonium is very high in proportion to U-238, reducing the magnitude of the Doppler-broadening feedback. The smaller surface to volume ratio in the large core may minimize leakage, further reducing the safety performance of this core. In analyzing the effect of core temperature on criticality, the thermal expansion of the steel structures, such as the core support system and the radial reflector, were not simulated. A meaningful analysis of these phenomena may be performed once the geometry of the core support structure is better known. Depending on whether the radial reflector expands inwards or outwards with an increase in temperature, the volume of salt in the active core could decrease or increase with an increase in power. In this way, the expansion of the core base plate could produce a substantial positive or negative effect on k_{eff} , depending on how it is engineered. However, the magnitude of this effect and the time-frame in which it would actuate during a transient event remain to be seen.

The minimum active core volume required to achieve criticality at equilibrium was found to be 50.3 m^3 , for a core radius of 200 cm and an in core average fuel lifetime (τ) of between 13.64 and 19.88 years (or equivalently, by achieving a discharge burnup of between 37% and 46% FIMA). Assuming an equilibrium natural-Uranium feedstock of NaCl-UCl₃ of molar ratio 50 at. % UCl₃ at a density of 3.48 g cm^{-3} , then this corresponds to a constant feed-rate of between 7465 kg and 5120 kg of natural Uranium per year.

One way to reduce the core volume is to enrich the feed material moderately, which may be necessary if such large core volumes are deemed infeasible [47]. However, such a compromise would somewhat negate the economic and proliferation-resistance advantages of the B&BMSR concept and may prove unacceptable for these reasons. A detailed study of this core volume (and core power) vs. feed-enrichment trade-off may be required to find an economic optimum in which the increased SWUs in fuel production is compared to construction and operational costs.

By reducing the heights of the reactor plena, the lifetimes of the upper and lower steel internals were prolonged. However, this design decision precluded the option of placing the heat exchangers and pumps in the upper plenum. Instead it seems best to place these components in the downcomer region, where the fluence would be substantially reduced by the presence of the radial reflector. In addition, neutron shielding material could be placed outside the radial reflector (as in the design of the MSFR) to further protect the heat exchangers and pumps. Indeed, shielding could be placed outside of the steel components in direct contact with the active core (i.e. the radial reflector, upper steel internals and lower steel internals) to shield the reactor vessel while having a minimal impact on criticality.

Appendices

Appendix A

Density Calculations

A.1 Lead Density Estimation

In these reflector size and material simulation tests, the density of liquid Lead was obtained from equation A.1 for a temperature of 800 °C [49].

$$\rho = 10.678 - 13.174 \times 10^{-4} \times (T - 600.6) \quad (\text{A.1})$$

where:

- ρ is the density of Lead in g cm^{-3} .
- T is the temperature of the Lead in Kelvin, chosen to be 1073.15 K, corresponding to a estimated reactor operating temperature of 800 °C.

A.2 Chloride Salt Densities

The density of UCl_3 and NaCl-UCl_3 systems of various molar fractions were calculated at the estimated reactor operating temperature from a density-temperature correlation for a UCl_3 molar % of 49.5% found in the literature [19], which took the form of equation A.2.

$$\rho = 4.4738 - 0.9304 \times 10^{-3} \times T \quad (\text{A.2})$$

where:

- ρ is the density of the NaCl-UCl_3 system in g cm^{-3} .
- T is the temperature of the salt in Kelvin.

A.3 HT9 Steel Density Estimation

A room temperature density value of $\rho_{RT} = 7.75 \text{gcm}^{-3}$ and an expression for the thermal expansion coefficient of HT9 steel (equation A.3) found in [44]. This allowed the density of HT9 at the potential operating temperature of the reactor to be estimated, as described below.

$$\alpha(T) = A + BT + CT^2 \quad (\text{A.3})$$

where:

- $A = 5.678 \times 10^{-6}$, $B = 1.6222 \times 10^{-8}$ and $C = -7.728 \times 10^{-12}$
- $\alpha(T)$ is the thermal expansion coefficient.
- T is the temperature of the material.

The thermal expansion coefficient is related to the density of a material through equation A.4.

$$\alpha = -\frac{\partial \ln(\rho)}{\partial T} \quad (\text{A.4})$$

where ρ is the density of the material.

By re-arranging this equation and integrating both sides an expression for the density of the HT9 steel at 800 °C was obtained as described in equations A.5 and A.6.

$$\int_{\ln(\rho_{RT})}^{\ln(\rho_T)} \partial(\ln(\rho)) = - \int_{RT}^T \alpha(T) \partial T \quad (\text{A.5})$$

$$\therefore \ln(\rho_T) - \ln(\rho_{RT}) = - \left[A * T + \frac{B * T^2}{2} + \frac{C * T^3}{3} \right]_{RT}^T$$

By rearranging equation A.5 and raising e to the power of both sides we can arrive at a value for the density of HT9 steel at the estimated operating temperature of the reactor.

$$\rho_T = \rho_{RT} * \exp \left(A * RT + \frac{B * RT^2}{2} + \frac{C * RT^3}{3} - A * T - \frac{B * T^2}{2} - \frac{C * T^3}{3} \right)$$

$$= 7.67 \text{ g cm}^{-3} \quad (\text{A.6})$$

Appendix B

Core Volume & Power Calculations

For all burnup simulations carried out (i.e. for sections 5.5 and 5.6) the reduced-plena-heights version of **Geometry B** was used as a template. The upper and lower plena heights were fixed at 5 cm. The downcomer thickness was fixed at 20 cm. The active core height was adjusted to be equal to twice the radius of the active core to minimize leakage. A 20 cm 90% steel/10% fuel-salt was used to represent the radial reflection. The upper and lower steel internals were represented by a 50% steel/50% fuel-salt region directly above and below the active core, whose radius was equal to the radius of the active core plus the thickness of the radial reflector.

The volume of salt in the active core can therefore be calculated from equation B.1.

$$V_{active} = 2\pi r_{core}^3 \quad (B.1)$$

The volume of the reflector region may be calculated from equation B.2.

$$V_{reflector} = \pi r_{reflector}^2 * h_{core} - V_{active} = 2\pi r_{core} * \left((r_{core} + 20)^2 - r_{core}^2 \right) \quad (B.2)$$

The volume of the upper and lower steel internals, both of height 5 cm, is given in equation B.3.

$$V_{SI} = \pi (r_{core} + 20)^2 (2r_{core} + 10) - V_{active} - V_{reflector} \quad (B.3)$$

Finally the total volume of salt in the core, excluding the mixed steel/salt reflector and steel internal regions, can be obtained from equation B.4 .

$$V_{salt,total} = \pi r_{DC}^2 h_{DC} - V_{SI} - V_{reflector} \quad (B.4)$$

Using these equations and by assuming a power density in the active core region of 300 W cm^{-3} , the total power of each core volume was calculated and provided as a normalization scaling factor for the corresponding Serpent simulation. This volume and thermal power data for each core radius simulated is provided in table B.1.

r_{core}	V_{active}	$V_{reflector}$	V_{SI}	$V_{salt,total}$	Power (GWth)
1.5	21.21	6.03	3.63	30.03	6.3617
1.6	25.74	6.84	4.07	35.59	7.7208
1.7	30.87	7.69	4.54	41.81	9.2608
1.8	36.64	8.60	5.03	48.72	10.9931
1.9	43.10	9.55	5.54	56.37	12.9289
2	50.27	10.56	6.08	64.79	15.0796
2.1	58.19	11.61	6.65	74.03	17.4566
2.2	66.90	12.72	7.24	84.11	20.0710
2.3	76.45	13.87	7.85	95.07	22.9343
2.4	86.86	15.08	8.49	106.96	26.0576
2.5	98.17	16.34	9.16	119.82	29.4524
2.6	110.43	17.64	9.85	133.67	33.1300
2.7	123.67	19.00	10.57	148.56	37.1016
2.8	137.93	20.41	11.31	164.52	41.3785
2.9	153.24	21.87	12.08	181.59	45.9722
3	169.65	23.37	12.87	199.82	50.8938

TABLE B.1: Core volume and power information, with radii and volumes in m and m³, respectively.

Bibliography

- [1] *A periodic table of the elements grouped by feed/removal rate in the modified version of Serpent.*
- [2] *Akkuyu Nuclear JSC AKKUYU NÜKLEER A.Ş.* URL: <http://www.akkunpp.com/akkuyu-nuclear-jsc> (visited on 06/14/2018).
- [3] David Albright. *French military plans for Superphenix?* en. Google-Books-ID: 1AUAAAAMBAJ. Nov. 1984, pp. 30–34.
- [4] Todd R Allen et al. “Radiation response of a 9 chromium oxide dispersion strengthened steel to heavy ion irradiation”. In: *Journal of Nuclear Materials* 375.1 (2008), pp. 26–37.
- [5] BPVC ASME III. “Section III-Rules for Construction of Nuclear Facility Components-Division 2-Code for Concrete Containments”. In: ASME. 2015.
- [6] M Aufiero et al. “An extended version of the SERPENT-2 code to investigate fuel burn-up and core material evolution of the Molten Salt Fast Reactor”. In: *Journal of Nuclear Materials* 441.1-3 (2013), pp. 473–486.
- [7] Mariya; Cammi Antonio; Clifford Ivor; Geoffroy Olivier; Heuer Daniel; Laureau Axel; Losa Mario; Luzzi Lelio; Merle-Lucotte Elsa; Ricotti Marco E.; Rouch Hervé Aufiero Manuele; Brovchenko. “Calculating the effective delayed neutron fraction in the Molten Salt Fast Reactor: Analytical, deterministic and Monte Carlo approaches”. In: *Annals of Nuclear Energy* 65 (Mar. 2014). DOI: [10.1016/j.anucene.2013.10.015](https://doi.org/10.1016/j.anucene.2013.10.015).
- [8] Mahmoud Bakr. “The Build-Own-Operate (BOO) approach: Advantages and challenges”. en. In: (). URL: https://www.academia.edu/17024655/The_Build-Own-Operate_BOO_approach_Advantages_and_challenges (visited on 08/11/2018).
- [9] A. A. Bauer and M. Kangilaski. “Helium generation in stainless steel and nickel”. In: *Journal of Nuclear Materials* 42.1 (Jan. 1972), pp. 91–95. ISSN: 0022-3115. DOI: [10.1016/0022-3115\(72\)90011-6](https://doi.org/10.1016/0022-3115(72)90011-6). URL: <http://www.sciencedirect.com/science/article/pii/0022311572900116> (visited on 07/02/2018).
- [10] O. Beneš and R. J. M. Konings. “Thermodynamic evaluation of the NaCl–MgCl₂–UCl₃–PuCl₃ system”. In: *Journal of Nuclear Materials* 375.2 (Apr. 2008), pp. 202–208. ISSN: 0022-3115. DOI: [10.1016/j.jnucmat.2008.01.007](https://doi.org/10.1016/j.jnucmat.2008.01.007). URL: <http://www.sciencedirect.com/science/article/pii/S002231150800010X> (visited on 08/05/2018).

- [11] Dietmar Bittermann, Ulrich Krugmann, and Garo Azarian. "EPR accident scenarios and provisions". In: *Nuclear Engineering and Design* 207.1 (2001), pp. 49–57. ISSN: 0029-5493. DOI: [https://doi.org/10.1016/S0029-5493\(00\)00425-8](https://doi.org/10.1016/S0029-5493(00)00425-8). URL: <http://www.sciencedirect.com/science/article/pii/S0029549300004258>.
- [12] Tom Boden and Bob Andres. *Global CO2 Emissions from Fossil-Fuel Burning, Cement Manufacture, and Gas Flaring: 1751-2014*. URL: http://cdiac.ess-dive.lbl.gov/ftp/ndp030/global.1751_2014.ems (visited on 06/06/2018).
- [13] Hubert Boussier. "Molten Salt Reactor System GIF 2011 Status". In: Generation IV International Forum. 2011. URL: [://www.iaea.org/NuclearPower/Downloads/INPRO/Meetings/GIF/5th%20Meeting/MSR%20Anzieu.pdf](http://www.iaea.org/NuclearPower/Downloads/INPRO/Meetings/GIF/5th%20Meeting/MSR%20Anzieu.pdf).
- [14] John Bussac and Paul Reuss. "Traité de neutronique: Physique et calcul des réacteurs nucléaires". In: (1978), pp. 582–583.
- [15] Yiren Chen. "IRRADIATION EFFECTS OF HT-9 MARTENSITIC STEEL". en. In: *Nuclear Engineering and Technology* 45.3 (June 2013), pp. 311–322. ISSN: 17385733. DOI: [10.5516/NET.07.2013.706](https://doi.org/10.5516/NET.07.2013.706). URL: <http://linkinghub.elsevier.com/retrieve/pii/S1738573315300176> (visited on 04/25/2018).
- [16] "Citizens' summary: EU plan for a competitive low-carbon economy by 2050". en. In: (), p. 2. URL: https://ec.europa.eu/clima/sites/clima/files/summary/docs/roadmap_2050_en.pdf.
- [17] Intergovernmental Panel on Climate Change and Ottmar Edenhofer, eds. *Climate change 2014: mitigation of climate change: Working Group III contribution to the Fifth Assessment Report of the Intergovernmental Panel on Climate Change*. en. OCLC: ocn892580682. New York, NY: Cambridge University Press, 2014. ISBN: 978-1-107-05821-7 978-1-107-65481-5.
- [18] Bill Corwin. "ASME Code Section III Division 5: Rules of Construction for High Temperature Reactors". In: Office of Advanced Reactor Technologies, Office of Nuclear Energy, U.S. Department of Energy. 2016. URL: <https://www.nrc.gov/public-involve/conference-symposia/adv-rx-non-lwr-ws/2016/06-corwin-asme.pdf>.
- [19] VN Desyatnik et al. "Density, surface tension, and viscosity of uranium trichloride-sodium chloride melts". In: *Soviet Atomic Energy* 39.1 (1975), pp. 649–651.
- [20] Mark Donohue. *Pokhran-I: India's First Nuclear Bomb*. 2011. URL: <http://large.stanford.edu/courses/2014/ph241/donohue1/> (visited on 06/07/2018).
- [21] N. D. Dudey, S. D. Harkness, and H. Farrar IV. "Helium Production in EBR-II Irradiated Stainless Steel". In: *Nuclear Applications and Technology* 9.5 (Nov. 1970), pp. 700–710. ISSN: 0550-3043. DOI: [10.13182/NT70-A28745](https://doi.org/10.13182/NT70-A28745). URL: <https://doi.org/10.13182/NT70-A28745> (visited on 07/03/2018).

- [22] SA Fabritsiev and VD Yaroshevich. "Mechanism of helium embrittlement of metals and alloys". In: *Strength of Materials* 18.9 (1986), pp. 1194–1202.
- [23] Šumit Ganguly. "India's Pathway to Pokhran II: The Prospects and Sources of New Delhi's Nuclear Weapons Program". In: *International Security* 23.4 (1999), pp. 148–177.
- [24] FA Garner, MB Toloczko, and BH Sencer. "Comparison of swelling and irradiation creep behavior of fcc-austenitic and bcc-ferritic/martensitic alloys at high neutron exposure". In: *Journal of Nuclear Materials* 276.1-3 (2000), pp. 123–142.
- [25] D.S. Gelles. "Microstructural examination of commercial ferritic alloys at 200 dpa". In: *Journal of Nuclear Materials* 233-237 (1996), pp. 293–298. ISSN: 0022-3115. DOI: [https://doi.org/10.1016/S0022-3115\(96\)00222-X](https://doi.org/10.1016/S0022-3115(96)00222-X). URL: <http://www.sciencedirect.com/science/article/pii/S002231159600222X>.
- [26] "German government wants nuclear exit by 2022 at latest". en. In: *Reuters* (May 2011). URL: <https://uk.reuters.com/article/us-germany-nuclear/german-government-wants-nuclear-exit-by-2022-at-latest-idUKTRE74Q2P120110530> (visited on 06/06/2018).
- [27] *GIF Portal - Home - Generation IV Goals*. URL: https://www.gen-4.org/gif/jcms/c_9502/generation-iv-goals (visited on 06/13/2018).
- [28] JG Gigax et al. "Radiation response of alloy T91 at damage levels up to 1000 peak dpa". In: *Journal of Nuclear Materials* 482 (2016), pp. 257–265.
- [29] M. R. Gilbert et al. "An integrated model for materials in a fusion power plant: transmutation, gas production, and helium embrittlement under neutron irradiation". en. In: *Nuclear Fusion* 52.8 (2012), p. 083019. ISSN: 0029-5515. DOI: [10.1088/0029-5515/52/8/083019](https://doi.org/10.1088/0029-5515/52/8/083019). URL: <http://stacks.iop.org/0029-5515/52/i=8/a=083019> (visited on 07/16/2018).
- [30] José Marcus Godoy, Maria Luiza DP Godoy, and Cláudia C Aronne. "Application of inductively coupled plasma quadrupole mass spectrometry for the determination of monazite ages by lead isotope ratios". In: *Journal of the Brazilian Chemical Society* 18.5 (2007), pp. 969–975.
- [31] Giacomo Grasso. "Neutronics analyses for fast spectrum nuclear systems and scenario studies for advanced nuclear fuel cycles". PhD thesis. alma, 2010.
- [32] Ehud Greenspan. *Physics of Breed and Burn Nuclear Reactors*. 2010. URL: http://www.gammaexplorer.com/wp-content/uploads/2017/03/Greenspan_TWR.pdf.
- [33] L. Greenwood. "SPECOMP Calculations of Radiation Damage in Compounds". In: *SPECOMP Calculations of Radiation Damage in Compounds*. 1989.

- [34] L. R. Greenwood. "A new calculation of thermal neutron damage and helium production in nickel". In: *Journal of Nuclear Materials* 115.2 (Apr. 1983), pp. 137–142. ISSN: 0022-3115. DOI: [10.1016/0022-3115\(83\)90302-1](https://doi.org/10.1016/0022-3115(83)90302-1). URL: <http://www.sciencedirect.com/science/article/pii/0022311583903021> (visited on 07/02/2018).
- [35] Lawrence R Greenwood and Robert K Smither. *SPECTER: Neutron damage calculations for materials irradiations*. Tech. rep. Argonne National Lab., IL (USA), 1985.
- [36] LR Greenwood and LS Kellogg. *Neutron Dosimetry for the MOTA-2A Experiment in FFTF*. Tech. rep. 1992.
- [37] M. L. Grossbeck and J. A. Horak. "Irradiation creep in type 316 stainless steel and us PCA with fusion reactor He/dpa levels". In: *Journal of Nuclear Materials* 155-157 (July 1988), pp. 1001–1005. ISSN: 0022-3115. DOI: [10.1016/0022-3115\(88\)90457-6](https://doi.org/10.1016/0022-3115(88)90457-6). URL: <http://www.sciencedirect.com/science/article/pii/0022311588904576> (visited on 07/07/2018).
- [38] Florent Heidet and Ehud Greenspan. "Neutron Balance Analysis for Sustainability of Breed-and-Burn Reactors". In: *Nuclear Science and Engineering* 171.1 (May 2012), pp. 13–31. ISSN: 0029-5639. DOI: [10.13182/NSE10-114](https://doi.org/10.13182/NSE10-114). URL: <https://doi.org/10.13182/NSE10-114> (visited on 08/06/2018).
- [39] PAVEL Hejzlar et al. "TERRAPOWER, LLC TRAVELING WAVE REACTOR DEVELOPMENT PROGRAM OVERVIEW". In: *Nuclear Engineering and Technology* 45.6 (Nov. 2013), pp. 731–744. ISSN: 1738-5733. DOI: [10.5516/NET.02.2013.520](https://doi.org/10.5516/NET.02.2013.520). URL: <http://www.sciencedirect.com/science/article/pii/S1738573315301753> (visited on 07/19/2018).
- [40] JC Hesson, MJ Feldman, and L Burris. *Description and proposed operation of the fuel cycle facility for the second experimental breeder reactor (EBR-II)*. Tech. rep. Argonne National Lab., Ill., 1963.
- [41] B Hombourger et al. "On the Feasibility of Breed-and-Burn Fuel Cycles in Molten Salt Reactors". en. In: *IAEA-CN245-388, Proceedings of International Conference on Fast Reactors and Related Fuel Cycles: Next Generation Nuclear Systems for Sustainable, Development FR17 conference* (), p. 10. URL: <https://media.superevent.com/documents/20170620/6c2493ec3ddb931737a0363f85a51b/fr17-388.pdf>.
- [42] P Hosemann et al. "Materials selection for nuclear applications: Challenges and opportunities". In: *Scripta Materialia* 143 (2018), pp. 181–187.
- [43] F. H. Huang. "Comparison of fracture behavior for low-swelling ferritic and austenitic alloys irradiated in the Fast Flux Test Facility (FFTF) to 180 DPA". In: *Engineering Fracture Mechanics* 43.5 (1992), pp. 733 – 748. ISSN: 0013-7944. DOI: [https://doi.org/10.1016/0013-7944\(92\)90004-X](https://doi.org/10.1016/0013-7944(92)90004-X). URL: <http://www.sciencedirect.com/science/article/pii/001379449290004X>.

- [44] Woan Hwang, HY Kang, BO Lee, et al. *Metallic fuel design development*. Tech. rep. Korea Atomic Energy Research Institute, 1999, p. 211.
- [45] IAEA *Country Nuclear Power Profiles: Germany 2017*. URL: <https://cnpp.iaea.org/countryprofiles/Germany/Germany.htm> (visited on 06/06/2018).
- [46] Michael G. Jenkins, Stephen T. Gonczy, and Yutai Katoh. "COMPOSITION, STRUCTURE, MANUFACTURE, AND PROPERTIES OF SIC-SIC CMCS FOR NUCLEAR APPLICATIONS: INFORMATIONAL CHAPTERS IN THE ASME BPV CODE SECTION III." In: *Ceramic Engineering & Science Proceedings* 37.6 (2016), p. 17. ISSN: 01966219. URL: <https://libproxy.berkeley.edu/login?qurl=http%3a%2f%2fsearch.ebscohost.com%2flogin.aspx%3fdirect%3dtrue%26db%3dedb%26AN%3d121489530%26site%3dedb-live>.
- [47] A Kasam and E Shwageraus. "Feasibility studies of a breed and burn molten salt reactor". In: *2017 International Congress on Advances in Nuclear Power Plants, ICAPP 2017-A New Paradigm in Nuclear Power Safety, Proceedings*. 2017.
- [48] GH Kinchin and RS Pease. "The displacement of atoms in solids by radiation". In: *Reports on progress in physics* 18.1 (1955), p. 1.
- [49] A. D. Kirshenbaum, J. A. Cahill, and A. V. Grosse. "The density of liquid lead from the melting". In: *Journal of Inorganic and Nuclear Chemistry* 22.1 (Dec. 1961), pp. 33–38. ISSN: 0022-1902. DOI: 10.1016/0022-1902(61)80226-1. URL: <http://www.sciencedirect.com/science/article/pii/0022190261802261> (visited on 08/05/2018).
- [50] R. L. Klueh et al. "Mechanical properties of neutron-irradiated nickel-containing martensitic steels: I. Experimental study". In: *Journal of Nuclear Materials* 357.1 (Oct. 2006), pp. 156–168. ISSN: 0022-3115. DOI: 10.1016/j.jnucmat.2006.05.048. URL: <http://www.sciencedirect.com/science/article/pii/S0022311506003400> (visited on 07/03/2018).
- [51] R. L. Klueh et al. "Mechanical properties of neutron-irradiated nickel-containing martensitic steels: II. Review and analysis of helium-effects studies". In: *Journal of Nuclear Materials* 357.1 (Oct. 2006), pp. 169–182. ISSN: 0022-3115. DOI: 10.1016/j.jnucmat.2006.05.049. URL: <http://www.sciencedirect.com/science/article/pii/S0022311506003412> (visited on 07/03/2018).
- [52] Apse V.A. Kulikov G.G. Shmelev A.N. and Kulikov E.G. "IMPROVING SAFETY OF FAST REACTOR WITH CORE REFLECTED BY MATERIAL OF HEAVY ATOMIC WEIGHT AND EXTREMELY LOW NEUTRON ABSORPTION". In: 2018.
- [53] L Leibowitz and RA Blomquist. "Thermal conductivity and thermal expansion of stainless steels D9 and HT9". In: *International journal of thermophysics* 9.5 (1988), pp. 873–883.

- [54] Jaakko Leppänen et al. "The Serpent Monte Carlo code: Status, development and applications in 2013". In: *Annals of Nuclear Energy* 82 (2015), pp. 142–150.
- [55] Amy L Luers et al. "How to Avoid Dangerous Climate Change". en. In: (), p. 34.
- [56] Ludovic Mathieu et al. "Possible configurations for the thorium molten salt reactor and advantages of the fast nonmoderated version". In: *Nuclear Science and Engineering* 161.1 (2009), pp. 78–89.
- [57] E. Merle-Lucotte et al. "Introduction to the Physics of Molten Salt Reactors". In: *Materials Issues for Generation IV Systems*. Ed. by Véronique Ghetta et al. Dordrecht: Springer Netherlands, 2008, pp. 501–521. ISBN: 978-1-4020-8422-5.
- [58] Ehud Greenspan Massimiliano Fratoni Michael Martin Manuele Auffero. "Feasibility of a Breed-and-Burn Molten Salt Reactor". In: *Recent Advancements in Liquid and Solid Molten Salt Reactors* (2017).
- [59] "Neutron-induced dpa, transmutations, gas production, and helium embrittlement of fusion materials". In: FIFTEENTH INTERNATIONAL CONFERENCE ON FUSION REACTOR MATERIALS 442 (). ISSN: 0022-3115.
- [60] MJ Norgett, MT Robinson, and IM Torrens. "A proposed method of calculating displacement dose rates". In: *Nuclear engineering and design* 33.1 (1975), pp. 50–54.
- [61] MJ Norgett, MT Robinson, and IM Torrens. "Standard Practice for Neutron Radiation Damage Simulation by Charged-Particle Irradiation". In: *Annual Book of ASTM Standards* (1975).
- [62] R O'Sullivan and J Laurie. "Moltex Energy's stable salt reactors". In: *Revue Generale Nucleaire* (2016), pp. 48–52.
- [63] SI Porollo et al. "Swelling and void-induced embrittlement of austenitic stainless steel irradiated to 73–82 dpa at 335–365 C". In: *Journal of nuclear materials* 258 (1998), pp. 1613–1617.
- [64] "Primary Radiation Damage in Materials". en. In: (2015), p. 87.
- [65] Staffan Qvist. "Optimizing the design of small fast spectrum battery-type nuclear reactors". In: *Energies* 7.8 (2014), pp. 4910–4937.
- [66] Edward A Read and Cassiano RE de Oliveira. "A functional method for estimating DPA tallies in Monte Carlo calculations of light water reactors". In: (2011).
- [67] Keywan Riahi et al. "Locked into Copenhagen pledges — Implications of short-term emission targets for the cost and feasibility of long-term climate goals". en. In: *Technological Forecasting and Social Change* 90 (Jan. 2015), pp. 8–23. ISSN: 00401625. DOI: [10.1016/j.techfore.2013.09.016](https://doi.org/10.1016/j.techfore.2013.09.016). URL: <http://linkinghub.elsevier.com/retrieve/pii/S0040162513002539> (visited on 06/06/2018).

- [68] Murray W Rosenthal. "An account of Oak Ridge National Laboratory's thirteen nuclear reactors". In: *ORNL/TM-2009/181, August* (2009).
- [69] H. Rouch et al. "Preliminary thermal-hydraulic core design of the Molten Salt Fast Reactor (MSFR)". In: *Annals of Nuclear Energy* 64 (Feb. 2014), pp. 449–456. ISSN: 0306-4549. DOI: [10.1016/j.anucene.2013.09.012](https://doi.org/10.1016/j.anucene.2013.09.012). URL: <http://www.sciencedirect.com/science/article/pii/S0306454913004829> (visited on 07/30/2018).
- [70] Pablo R. Rubiolo et al. "High temperature thermal hydraulics modeling of a molten salt: application to a molten salt fast reactor (MSFR)". en. In: *ESAIM: Proceedings and Surveys* 58 (2017). Ed. by Stéphane Delacherie et al., pp. 98–117. ISSN: 2267-3059. DOI: [10.1051/proc/201758098](https://doi.org/10.1051/proc/201758098). URL: <http://www.esaim-proc.org/10.1051/proc/201758098> (visited on 05/24/2018).
- [71] Mycle Schneider. "Fast Breeder Reactors in France". en. In: *Science & Global Security* 17.1 (June 2009), pp. 36–53. ISSN: 0892-9882, 1547-7800. DOI: [10.1080/08929880902953013](https://doi.org/10.1080/08929880902953013). URL: <http://www.tandfonline.com/doi/abs/10.1080/08929880902953013> (visited on 06/09/2018).
- [72] T.L. Schulz. "Westinghouse AP1000 advanced passive plant". In: *Nuclear Engineering and Design* 236.14 (2006). 13th International Conference on Nuclear Energy, pp. 1547–1557. ISSN: 0029-5493. DOI: <https://doi.org/10.1016/j.nucengdes.2006.03.049>. URL: <http://www.sciencedirect.com/science/article/pii/S0029549306003190>.
- [73] Hiroshi Sekimoto, Kouichi Ryu, and Yoshikane Yoshimura. "CANDLE: the new burnup strategy". In: *Nuclear science and engineering* 139.3 (2001), pp. 306–317.
- [74] B.H. Sencer et al. "Microstructural analysis of an HT9 fuel assembly duct irradiated in FFTF to 155dpa at 443 C". en. In: *Journal of Nuclear Materials* 393.2 (Sept. 2009), pp. 235–241. ISSN: 00223115. DOI: [10.1016/j.jnucmat.2009.06.010](https://doi.org/10.1016/j.jnucmat.2009.06.010). URL: <http://linkinghub.elsevier.com/retrieve/pii/S0022311509006710> (visited on 06/12/2018).
- [75] M Sene. "Superphenix: the reality behind the myth". In: *Ecologist (London)* 16.4-5 (1986), pp. 198–200.
- [76] José A Seneda et al. "Study on radiogenic lead recovery from residues in thorium facilities using ion exchange and electrochemical process". In: *Progress in Nuclear Energy* 52.3 (2010), pp. 304–306.
- [77] Special Metals Material Data Sheet. "Inconel alloy 617". In: 2016. URL: <http://www.specialmetals.com/assets/smc/documents/alloys/inconel/inconel-alloy-617.pdf>.
- [78] John Taylor. *Introduction to error analysis, the study of uncertainties in physical measurements*. 1997.
- [79] LLC TerraPower. "Traveling-wave reactors: a truly sustainable and full-scale resource for global energy needs". In: *Proceeding of ICAPP*. Vol. 2010. 2010.

- [80] MB Toloczko, FA Garner, and CR Eiholzer. "Irradiation creep and swelling of the US fusion heats of HT9 and 9Cr-1Mo to 208 dpa at 400 C". In: *Journal of Nuclear Materials* 212 (1994), pp. 604–607.
- [81] Gary S Was. *Fundamentals of radiation materials science: metals and alloys*. Springer, 2016.
- [82] David Wootan. *MCNPX Calculation of DPA*. 2014. URL: <https://radiate.fnal.gov/meetings/WootanDPA.pdf>.
- [83] Hongjie Xu, Zhimin Dai, and Xiangzhou Cai. "Some Physical Issues of the Thorium Molten Salt Reactor Nuclear Energy System". en. In: *Nuclear Physics News* 24.2 (Apr. 2014), pp. 24–30. ISSN: 1061-9127, 1931-7336. DOI: 10.1080/10619127.2014.910434. URL: <http://www.tandfonline.com/doi/abs/10.1080/10619127.2014.910434> (visited on 08/10/2018).
- [84] Guanheng Zhang, Massimiliano Fratoni, and Ehud Greenspan. "Advanced Burner Reactors with Breed-and-Burn Thorium Blankets for Improved Economics and Resource Utilization". In: *Nuclear Technology* 199.2 (2017), pp. 187–218. DOI: 10.1080/00295450.2017.1337408. eprint: <https://doi.org/10.1080/00295450.2017.1337408>. URL: <https://doi.org/10.1080/00295450.2017.1337408>.
- [85] Guanheng Zhang et al. "Preliminary Study of Advanced Sodium-Cooled Burner Reactors with External and Internal Thorium Blankets". en. In: *Transactions of the American Nuclear Society* 111 (2014), p. 7.
- [86] James F Ziegler, Matthias D Ziegler, and Jochen P Biersack. "SRIM—The stopping and range of ions in matter (2010)". In: *Nuclear Instruments and Methods in Physics Research Section B: Beam Interactions with Materials and Atoms* 268.11-12 (2010), pp. 1818–1823.

Summary

A Breed-and-Burn Molten Chloride Fast Reactor (B&BMCFR) was designed and simulated in a modified version of the Serpent Monte Carlo code which allowed for a continuous stream of material to flow into the core as the burn-up simulation progressed. Several combinations of radial reflector material and thickness were simulated and their neutronic impact assessed. A mix of 90% HT9 steel and 10% fuel salt was chosen for further evaluation as a radial reflector. In this material, the reflection of neutrons was observed to saturate at a thickness of approximately 20 cm, providing a $\Delta k_{eff} = +1415.1 \pm 127.8$ pcm.

The lifetime of steel materials against radiation damage was estimated using a limit of 208 Displacements Per Atom (DPA). The shortest lifetime of all components was estimated to be 1 year for the Upper Steel Internals (USI) region. By reducing the volume of salt in the upper and lower plena, this USI lifetime was extended to 3 years, which remains too low to be practical. This change to the reactor plena also reduced k_{eff} by 690 ± 93 pcm, equivalent to $\sim 49\%$ of the increase in k_{eff} observed with the addition of the 20 cm HT9 steel radial reflector. Efforts to raise the radiation damage constraint for steels above ~ 208 DPA were discussed, as were new accident-tolerant structural materials.

Helium build-up was modeled in steel components, but it was concluded that the initial concentration of Nickel in HT9 steel is too low for neutron capture in Nickel isotopes to produce the critical embrittlement concentration for Iron of 764.6 appm. Therefore DPA was chosen to be the primary means of estimating component lifetimes in this study.

The safety of the reactor was partially assessed by estimation of the temperature reactivity coefficient. α_{temp} was estimated for a range of core radii and feed/removal rates of actinides and fission products from the core. It was found to be negative for all of the parameter space simulated, with a general trend of increasing α_{temp} with decreasing feed/removal rate and increasing core radius. The minimum active core volume for which breed-and-burn could be sustained was found to be 50.3 m^3 corresponding to a total fuel-salt volume of 64.8 m^3 and a total power of 15.08 GWth, assuming an active-core power density of 300 W cm^{-3} . The temperature-reactivity coefficient for this core was estimated to be $-5.8 \pm 0.2 \text{ pcm K}^{-1}$. Pb-208 was discussed as a potential reflector material for its superior neutron reflection properties and its ability to slow down and reduce the magnitude of the power increase during transient events.

While theoretically possible, substantial technical challenges must be overcome in order for the operation of an MCFR in the B&B mode to be practical. Specifically, the very short component lifetimes against radiation damage and the large core volumes necessary to sustain criticality must both be improved for the B&BMCFR to have economic potential. However, if these challenges are met, this design may be unique in achieving all of the Gen IV goals of economic feasibility, environmental sustainability, enhanced safety and proliferation-resistance.